Effect of Engine Thrust and I_{sp} Tradeoffs and Alternate Propellants on ΔV Budget and Architecture Mass for 1st Generation Nuclear Thermal Propulsion Flight Test Systems

Daria Nikitaeva[1] and Matthew Duchek[2]

[1] *Aerospace Systems Engineer, Advanced Projects, Analytical Mechanics Associates, Huntsville, AL, 35806*

[2] *Aerospace Engineering Manager, Advanced Projects, Analytical Mechanics Associates, Denver, CO, 80211*

ABSTRACT

Following the first Nuclear Thermal Propulsion (NTP) system test, also known as DRACO, the next NTP system to be developed would be the 1st Generation NTP system. An analysis was conducted to determine the performance of different vehicle configurations utilizing hydrogen (H-NTP), ammonia (A-NTP), and methane (M-NTP) as propellants launched onboard commercial launch vehicles. This was enabled by a quasi-steady-state power balance engine model and vehicle component physics that sized the vehicle system using Master Equipment List (MEL) parameters. The analysis considered configuration cases outlined by a matrix of different mission classes and vehicle configurations that covered the design space of the 1st Generation NTP system to explore various propellant options, engine architectures, and mission scopes.

Four mission classes were evaluated which included single burn missions performing maneuvers having a ΔV of 1 km/s and 2.5 km/s followed by 2-burn and 4-burn missions that aimed to exhaust the launch vehicles volume or mass limitations. In all cases, the NTP systems with the lowest thrust class had the longest burn time of which A-NTP and M-NTP systems provided the longest and shortest burn times depending on the launch vehicle used while H-NTP systems tended to cluster together in the middle. Longer burn times could be useful as a testing platform to increase the time for data accumulation. Across the multi-burn cases, H-NTP systems were found to be volume limited while A-NTP and M-NTP systems were mass limited. Both single burn missions showed that A-NTP configurations provided the lowest dry mass given that ammonia had the highest density with comparable performance to M-NTP systems and no requirement for cryocoolers. The results showed that beyond the propellant selection type, the launch vehicle selection, which included Starship, New Glenn, Vulcan, Falcon 9 (recoverable), and Falcon Heavy (recoverable), was a primary driving factor in the test vehicle's capabilities.

Trends were determined based on a set of dimensionless parameters that included the mass ratio of inert mass to initial wetted mass, ratio of specific impulse to burn time, and a dimensionless engine parameter (ratio of impulse to engine momentum). These relationships found the "knees-in-the-curves" that could be a significant point of reference for the designer as they indicate a change in the trend which is located at a specific impulse to burn time ratio of 1, a mass ratio of 0.6, and an engine performance parameter of 4. This study did not attempt to make a recommendation rather provide the tools for the reader to select their own configuration based on their needs.

I. INTRODUCTION/BACKGROUND

Nuclear Thermal Propulsion (NTP) is an in-space propulsion method which underwent significant development in the United States 1950s through the early 1970s during the Project Rover and Nuclear Engine for Rocket Vehicle Application (NERVA) programs. The goal of these two programs was to create a propulsion system capable of transporting humans to Mars and provide a reusable Lunar shuttle. Unlike chemical propulsion, NTP does not depend on combustion of an oxidizer and fuel to produce thrust; instead, a propellant is pumped into a nuclear reactor and heated to high temperatures before being expelled through a nozzle. Essentially, the NTP-based engine is a monopropellant system [1]. This allows for the theoretical use of any fluid to be used as a propellant if it is compatible with the neutronics inside the reactor and the materials do not exhibit significant degradation throughout the useful life of the engine at the high temperatures and pressures that are typically found inside the reactor core.

Current efforts are underway by NASA and DARPA to flight test the first NTP engine which will be followed by the 1st Generation NTP engine system. This system is envisioned to be tested both with a ground test capability and in a flight demonstration. Testing and associated modeling and simulation must be sufficient that Generation 1 leads to a Generation 2 operational NTP engine system. Generation 2 is envisioned to be the first mission-operational NTP system, with applications in cis-Lunar space. From experience gained there, a human-rated Mars-capable system could be developed.

Hydrogen is commonly considered as a propellant for NTP engines due to its low molecular weight which maximizes the benefit of the monopropellant capability by maximizing the achievable specific impulse (a measure of propellant efficiency in rocket engines). Hydrogen-based NTP engines in literature have been referred to as H-NTP. Although hydrogen has some favorable properties such as very low molecular weight and a critical point with relatively low pressure and temperature (1.3 MPa and 33 K, respectively), it has high specific heat capacity and low density, which exhibit drawbacks in both an engine and space transportation vehicle context, respectively.

Alternate propellant NTP engines were considered to address hydrogen's high specific heat capacity and low density which included Ammonia-based NTP (A-NTP) [2] and Methane-based NTP (M-NTP) engines [3]. However, these two propellants could have other drawbacks in the form of required dissociation/thermolysis/pyrolysis energy which will drive the reactor power up or chamber temperature down. This is especially a concern for methane where its kinetics are short, and studies revealed that heavier compounds could be polymerized from methane radicals remaining after partial pyrolysis. This is not as much of a concern for ammonia as its thermolysis kinetics are long. Nevertheless, to capture the entire engine operating range in terms of specific impulse, based on prior work [2–5], A-NTP range is assumed to be between 375 sec and 450 sec while M-NTP range is assumed to be between 350 sec and 494 sec. M-NTP has a wider range given a large breadth of potential species and resulting chamber temperatures that could result from pyrolysis [3].

II. SPACECRAFT ARCHITECTURE MODEL OVERVIEW

The methodology employed for evaluating NTP vehicle architectures begins with determining the mission architecture along with the required ΔV, typically modeled in Copernicus [6]. Engine performance estimates were obtained from a modular, propellant and cycle flexible high fidelity engine model coded in Simulink with coupled neutronics through OpenMC called the X-NTP model which was documented in detail in previous work [2,4]. This model is capable of not only providing steady state performance metrics but also quasi-steady-state engine performance parameters that can be made to be functions of any other one parameter that is outputted from the model. When the quasi-steady-state performance database is coupled with temporal derivatives or relations between parameters, the quasi-steady-state database yields transient engine performance which could be used inside an Architecture model which is used to simulate and optimize the spacecraft and its architecture given a set of mission specified ΔV values, payload drop schedule, and quasi-steady-state engine parameter datasets as well as specified vehicle structure and methods of optimization [5]. Further development of this model includes a Master Equipment List (MEL) that scales according to the stage size and launch vehicles considered. This paper provides a detailed walkthrough of the MEL-integrated Architecture model which is then used to perform an analysis on different engine/propellant configurations, launch vehicles, and ΔV/number of burns for a flight test of a 1st Generation NTP engine. The considered matrix of cases will be shown and discussed in Section III.

II.A. Master Equipment List Physics Models

The Master Equipment List (MEL) is coded in MATLAB and has several modules that support the calculations of the structural/dry mass of the vehicle. The modules that support the MEL can be broken down into two types: (1) Physics Calculations and (2) Constants/Assumptions set up. The MEL then incorporates these separate modules into a coherent model that runs optimization based on the launch vehicle selection and orbit. This section breaks down these modules and describes them followed by a description of their integration and use in the Architecture model.

II.A.1 Battery

The battery mass module takes the required power draw P_{req} and sizes the battery accordingly to obtain the mass of the batteries m_{bat}. The first calculation is the determination of the total degradation factor D_F based on the degradation rate D_R and the lifetime l of the battery via Eq. 1. Using D_F, the useable capacity E_{use} can be found from P_{req}, power margin P_{mar}, battery efficiency η_{bat}, and the number of batteries n_{bat} through the relation shown in Eq. 2. Then the total capacity E_{tot} is found by incorporating the battery discharge depth d_d as shown in Eq. 3. The power density ρ_{pwr}, which is the power per kilogram, is then used to find m_{bat} as shown in Eq. 4. The assumed power densities and battery types that are implied are shown in Table 1.

$$D_F = \left(1 - \frac{D_R}{100}\right)^l \qquad \text{Eq. 1}$$

$$E_{use} = \frac{P_{req}(1 + P_{mar})}{\eta_{bat} D_F n_{bat}} \qquad \text{Eq. 2}$$

$$E_{tot} = \frac{E_{use}}{d_d} \qquad \text{Eq. 3}$$

$$m_{bat} = \frac{E_{tot}}{\rho_{pwr}} n_{bat} \qquad \text{Eq. 4}$$

Table 1: Battery Types and Power Densities

Battery Type	**Power Density (W-hr/kg)**
Ni-CD	30
Ni-H2	60
Li-ion	125

II.A.2 Bus Structure

The Bus Structure module is assumed to be the skirt that extends beyond the propellant tank and houses various components for that stage with a single output that provides the mass of the bus structure m_{bus}. The arguments that this module accepts are the launch vehicle selection and number of docking ports. The bus structure is modeled as a solid body made of a selected material (or a structure with openings and an average density) in the shape of an open cylinder without end caps. The volume is found by using an assumed thickness thin-shelled cylinder which can be converted into mass through a material density. Furthermore, if a stage docks at both ends, there is a cylindrical bus at both ends and vice versa.

II.A.3 Communications/Command & Data-Handling Systems/Guidance, Navigation, & Control

The Communications/Command & Data-Handling Systems/Guidance, Navigation, & Control (C/CDH/GNC) module simply loads the setup parameters for the different components and sums the different power levels to get the total power required. For the masses, each mass $m_{\mathrm{C/CDH/GNC}_i}$ is modified by the mass growth allowance MGA_i (in percent) for each individual component and all of them are summed together for the total mass of this system $m_{\mathrm{C/CDH/GNC}_{tot}}$ as shown in Eq. 7.

$$m_{\mathrm{C/CDH/GNC}_{tot}} = \sum_{i=1}^{n} \left[m_{\mathrm{C/CDH/GNC}_i} \left(1 + \frac{MGA_i}{100} \right) \right] \quad \text{Eq. 7}$$

II.A.4 Cryogenic Fluid Management

The Cryogenic Fluid Management (CFM) module determines not only the subsystem mass m_{CFM} but also the cryocooler input power $\dot{W}_{CFM}$ and the heat $\dot{Q}_{CFM}$ that must be rejected by the radiators. The total heat leak into the tank from structures and through the tank surface area is estimated based on a detailed thermal model of the structural leak paths and as a function of the tank surface area $A_{s_{tank}}$ and the CFM configuration (can be active, passive, or reduced boil-off) [7]. This heat leak is the heat lift ($\dot{Q}_T$) required of the cryocoolers. There may be cryocoolers operating at the tank surface, at a cooling layer embedded in the insulation system, or both. The subscript T represents at which temperature the heat is being lifted. The heat lifted and the power required at each cooling temperature is therefore summed to determine the total. The total heat lifted by the cryocoolers ($\dot{Q}_{lifted}$) is calculated by Eq. 8. Cryocooler performance is characterized by the input power needed per Watt of refrigeration power (P_{ratio}) at the operating cold temperature. The power required for a cryocooler at a temperature T is calculated by Eq. 9.

The masses of the secondary cryogenic system components, multi-insultation layer (MLI), spray-on foam insulation (SOFI), and structural MLI are calculated using the setup parameters for CFM. The secondary components mass m_S includes an allocation for cryo-mixers m_{mix} and sensors $m_{sensors}$ as well as radio frequency mass gauging (RFMG) m_{RFMG} and tank support MLI

m_{TSMLI} with the formulation shown in Eq. 10. The mass of the actual MLI m_{MLI} is determined by the number of MLI layers n_{MLI}, areal density of the MLI layers ρ_{MLI} in $\mathrm{kg/m^2}$, and $A_{s_{tank}}$ as shown in Eq. 11. The mass of SOFI m_{SOFI} is determined by the thickness of SOFI t_{SOFI}, density of SOFI ρ_{SOFI}, and $A_{s_{tank}}$ which is shown in Eq. 12. The structural MLI mass $m_{MLI_{struct}}$ depends on the number of structural MLI layers $n_{MLI_{struct}}$, specific mass of the structural MLI $\rho_{MLI_{struct}}$ in $\mathrm{kg/m^2}$, and $A_{s_{tank}}$ which is shown in Eq. 13. [7]

$$\dot{Q}_{lifted} = \sum_{T=T_1}^{n} (\dot{Q}_T) \qquad \text{Eq. 8}$$

$$\dot{W}_T = P_{ratio_T} \dot{Q}_T \qquad \text{Eq. 9}$$

$$m_S = m_{RFMG} + m_{mix} + m_{sensors} + m_{TSMLI} \qquad \text{Eq. 10}$$

$$m_{MLI} = n_{MLI} \rho_{MLI} A_{s_{tank}} \qquad \text{Eq. 11}$$

$$m_{SOFI} = t_{SOFI} A_{s_{tank}} \rho_{SOFI} \qquad \text{Eq. 12}$$

$$m_{MLI_{struct}} = n_{MLI_{struct}} \rho_{MLI_{struct}} A_{s_{tank}} \qquad \text{Eq. 13}$$

The CC masses, $\dot{W}_{CFM}$, and $\dot{Q}_{CFM}$ are calculated depending on the CFM configuration chosen. [7] The CC mass m_{CC} is determined by the CC specific mass at a temperature (m_{sp_T}), the heat lift capability $\dot{Q}_T$, m_{sp_T}, and the CC redundancy R_{CC} as shown in Eq. 14. The mass of the broad area cooling (BAC) m_{BAC} is dependent on the areal tube density of the tubes on the tank ρ_{t_i}, the tube and shield areal density outside the tank ρ_{st_o}, and $A_{s_{tank}}$ which is shown in Eq. 15. The total power of the active CFM $\dot{W}_{CFM}$ is provided by summation of the input power at each cryocooler temperature $\dot{W}_T$ as shown in Eq. 16. The total heat required to be rejected by the radiators from the CC ($\dot{Q}_{CFM}$) is the summation of $\dot{W}_{CFM}$ and $\dot{Q}_{lifted}$ as shown in Eq. 17. [7]

$$m_{CC} = \sum_{T=T_1}^{n} \left(m_{sp_T} \dot{Q}_T R_{CC}\right) \qquad \text{Eq. 14}$$

$$m_{BAC} = \left(\rho_{t_i} + \rho_{st_o}\right) A_{s_{tank}} \qquad \text{Eq. 15}$$

$$\dot{W}_{CFM} = \sum_{T=T_1}^{n} (\dot{W}_T) \qquad \text{Eq. 16}$$

$$\dot{Q}_{CFM} = \dot{W}_{CFM} + \dot{Q}_{lifted} \qquad \text{Eq. 17}$$

This mode returns a CFM mass, power, and heat rejected as 0. [7] The passive CFM mode calculates a CFM mass for insulation with power and heat rejected as zero watts. The reduced boil-off mode considers active cooling in a 90 K BAC shield only, and not at the 20 K tank surface and calculates the mass based on the higher temperature CFM using Eq. 14 through Eq. 17. [7]

II.A.5 Engine

The engine component calculates the total mass of the engine m_{eng} as well as the electrical power requirements given engine subcomponent masses, start up/shut down times, and burn time lengths. The average power required for engine operations $\dot{W}_{avg}$ are based on the engine peak and idle power ($\dot{W}_{peak}$ and $\dot{W}_{id}$), time at peak and idle power (t_{peak} and t_{id}), and the number of burns n_{burn} with the relation shown in Eq. 18. The energy of each burn E_{burn} depends on $\dot{W}_{peak}$; start up, steady state, shut down, and cooldown times (t_{su}, t_{ss}, t_{sd}, and t_{cd}); start up, steady state, shut down, and cooldown power factors (f_{su}, f_{ss}, f_{sd}, and f_{cd}) as shown in Eq. 19. The idle energy E_{id} required is based on t_{id} and $\dot{W}_{id}$ as shown in Eq. 20. The single burn cycle energy E_{cycle} is summation of E_{burn} and E_{id} as shown in Eq. 21 and the total mission energy $E_{mission}$ depends on E_{cycle}, n_{burn}, and number of engines n_{eng} as shown in Eq. 22. The total burn time t_{burn} depends on t_{su}, t_{ss}, t_{sd}, and t_{cd} as shown in Eq. 23. The burn power required $\dot{W}_{burn}$ to operate all the engines depends on E_{burn}, t_{burn}, and n_{eng} as shown in Eq. 24.

$$\dot{W}_{avg} = \frac{\dot{W}_{peak} t_{peak} n_{burn} + \dot{W}_{id} t_{id}}{t_{peak} + t_{id}} \quad \text{Eq. 18}$$

$$E_{burn} = \dot{W}_{peak}(f_{su}t_{su} + f_{ss}t_{ss} + f_{sd}t_{sd} + f_{cd}t_{cd}) \quad \text{Eq. 19}$$

$$E_{id} = \dot{W}_{id} t_{id} \quad \text{Eq. 20}$$

$$E_{cycle} = E_{id} + E_{burn} \quad \text{Eq. 21}$$

$$E_{mission} = \left(E_{cycle} n_{burn} + E_{id}\right) n_{eng} \quad \text{Eq. 22}$$

$$t_{burn} = t_{su} + t_{ss} + t_{sd} + t_{cd} \quad \text{Eq. 23}$$

$$\dot{W}_{burn} = \frac{E_{burn}}{t_{burn}} n_{eng} \quad \text{Eq. 24}$$

The total engine mass m_{eng} is the summation of user defined subcomponent masses which include the reactor $m_{reactor}$, engine hardware $m_{hardware}$, nozzle m_{nozzle}, nozzle extension m_{ext}, propellant ducting m_{duct}, external shield m_{shield}, and n_{eng} as shown in Eq. 25.

$$m_{eng} = (m_{reactor} + m_{hardware} + m_{nozzle} + m_{ext} + m_{duct} + m_{shield}) n_{eng} \quad \text{Eq. 25}$$

II.A.6 Docking and Thrust Structure

The docking and thrust structure modules calculate the mass of the connecting beams that hold the structures in place with the spacecraft mass, launch vehicle selection, and number of supported structures as inputs. The lateral loads F_{lat} depend on the spacecraft mass m_{SC}, the maximum lateral G's the launch vehicle will exhibit laterally G_{lat}, and a factor of safety FS as well as the gravitational constant g of 9.807 m/s^2 as shown in Eq. 26. The radius of the bus r_{bus} is assumed to be three quarters of the maximum payload radius. Since only the maximum and minimum payload diameters are known, $d_{pay_{max}}$ and $d_{pay_{min}}$, respectively, the bus radius becomes what is shown in Eq. 27, which is based on $d_{pay_{max}}$. The assumptions are true for the adapter radius r_{adapt}, except that it uses $d_{pay_{min}}$ as shown in Eq. 28. In both Eq. 27 and Eq. 28, the parameter C is a scaling value that has been assumed to be 0.75 for the docking structure and 0.95 for the thrust structure. The length of each beam L_{beam} is determined through trigonometry with the bus height H being the length parameter and the difference between r_{adapt} and r_{bus} being the width parameter as shown in Eq. 29 through the Pythagorean theorem. The angle that the beam makes with the base of the payload bay θ is dependent on the difference between r_{adapt} and r_{bus} as well as L_{beam} as shown in Eq. 30. The lateral force experienced by the beams $F_{beam_{lat}}$ is dependent on F_{lat}, θ, and the difference between r_{adapt} and r_{bus} with the relation shown in Eq. 31.

$$F_{lat} = m_{SC} g G_{lat} FS \quad \text{Eq. 26}$$

$$r_{bus} = \frac{d_{pay_{max}}}{2} C \quad \text{Eq. 27}$$

$$r_{adapt} = \frac{d_{pay_{min}}}{2} C \quad \text{Eq. 28}$$

$$L_{beam} = \sqrt{\left(r_{bus} - r_{adapt}\right)^2 + H^2} \quad \text{Eq. 29}$$

$$\theta = \cos^{-1}\left(\frac{r_{bus} - r_{adapt}}{L_{beam}}\right) \quad \text{Eq. 30}$$

$$F_{beam_{lat}} = \frac{F_{lat}}{\left(r_{bus} - r_{adapt}\right)\sin(\theta)} \quad \text{Eq. 31}$$

The axial load from the launch vehicle F_{axial} is determined from m_{SC}, the maximum launch vehicle axial G's G_{axial}, g, and FS as shown in Eq. 32. The axial load on the beam $F_{beam_{axial}}$ is dependent on F_{axial}, number of beams n_{beam}, and θ as shown in Eq. 33. Notice that $F_{beam_{lat}}$ does not depend on the number of beams as the maximum lateral force would be all the applied force loaded on to one beam. The maximum compressive load on any one beam F_{beam} is the sum of $F_{beam_{axial}}$ and $F_{beam_{lat}}$ as shown in Eq. 34. The minimum area that is required per beam A_{beam} is dependent on F_{beam} and the yield strength of the material $\sigma_{Y_{mat}}$ as shown in Eq. 35. Assuming that each beam has a circular cross-sectional area, the radius of the beam based on area r_{beam_A} is provided by Eq. 36. The second moment of inertia II of the beam is dependent on F_{beam}, ultimate factor of safety UFS, L_{beam}, and the modulus of elasticity of the material E_{mat} as shown in Eq. 37. The resulting beam radius from II, $r_{beam_{II}}$, is shown in Eq. 38. The maximum beam radius $r_{beam_{max}}$ is selected from r_{beam_A} and $r_{beam_{II}}$. The resulting beam volume $\forall_{beam}$ is determined from $r_{beam_{max}}$ and L_{beam} as shown in Eq. 39. The total mass of all the beams for the structure m_{struct} is dependent on $\forall_{beam}$, n_{beam}, and the density of the material ρ_{mat} as shown in Eq. 40.

$$F_{axial} = m_{SC} g G_{axial} FS \quad \text{Eq. 32}$$

$$F_{beam_{axial}} = \frac{F_{axial}}{n_{beam}\sin(\theta)} \quad \text{Eq. 33}$$

$$F_{beam} = F_{beam_{lat}} + F_{beam_{axial}} \quad \text{Eq. 34}$$

$$A_{beam} = \frac{F_{beam}}{\sigma_{Y_{mat}}} \quad \text{Eq. 35}$$

$$r_{beam_A} = \sqrt{\frac{A_{beam}}{\pi}} \quad \text{Eq. 36}$$

$$II = \frac{F_{beam} L_{beam}^2 UFS}{2\pi^2 E_{mat}} \quad \text{Eq. 37}$$

$$r_{beam_{II}} = \left(\frac{2II}{\pi}\right)^{1/4} \quad \text{Eq. 38}$$

$$\forall_{beam} = \pi r_{beam_{max}}^2 L_{beam} \quad \text{Eq. 39}$$

$$m_{struct} = \forall_{beam} \rho_{mat} n_{beam} \quad \text{Eq. 40}$$

II.A.7 Main Propellant Tank

The Main Propellant Tank Module considers the length of the different components that contribute to the overall length of the spacecraft such as the engine, bus, and thrust structures and outputs tank parameters such as dry tank mass $m_{tank_{dry}}$, tank surface area $A_{s_{tank}}$, and the total wetted tank mass m_{tank}. The length limit of the spacecraft is the useable payload length of the payload bay of the selected launch vehicle. The tank diameter d_{tank} is the useable payload diameter d_{pay} of the launch vehicle with a specified insultation thickness t_{ins}, that could be informed by other parameters of CFM, subtracted as shown in Eq. 41 which can be converted to a tank radius r_{tank}. It is assumed that the tank shape is cylindrical with ellipsoid shaped domes on the ends. The dome height h_{dome} is taken to be a function of r_{tank} and the relation is shown in Eq. 42. The volume of the dome $\forall_{dome}$, which is half an ellipsoid, is based on r_{tank} and h_{dome} with the relation shown in Eq. 43. The surface area of the dome $A_{s_{dome}}$ is also based r_{tank} and h_{dome} as well as a user defined ellipsoidal parameter p for which the relation is shown in Eq. 44.

$$d_{tank} = d_{pay} - 2t_{ins} \rightarrow r_{tank} = \frac{d_{tank}}{2} \quad \text{Eq. 41}$$

$$h_{dome} = \frac{\sqrt{2}}{2} r_{tank} \quad \text{Eq. 42}$$

$$\forall_{dome} = \frac{2}{3} r_{tank}^2 h_{dome} \quad \text{Eq. 43}$$

$$A_{s_{dome}} = 2\pi \left[\frac{1}{3}\left(r_{tank}^{2p} + 2r_{tank}^{p} h_{dome}^{p}\right)\right]^{1/p} \quad \text{Eq. 44}$$

The total length of the tank L_{tank} is dictated by the payload mass and volume capabilities of the launch vehicle for the selected orbit. A volume limited payload is one that utilizes the entire payload bay length L_{pay} while also accounting for the lengths of other components of the spacecraft such as the bus structure L_{bus}, docking structure L_{dock}, thrust structure L_{thrust}, and engine L_{eng}. Other parameters that dictate how the component lengths are used include the number of docking ports n_{dock} and if the spacecraft has engines (B_{eng}, which is a Boolean operator). All this is put together and shown in Eq. 45 for the volume limited tank length $L_{tank_{\forall}}$. The tank length of a mass limited payload L_{tank_m} will ALWAYS be lower than or equal to $L_{tank_{\forall}}$ and L_{tank_m} is iteratively adjusted according to the comparison of the launch vehicle payload mass capabilities and the resulting total spacecraft mass as discussed in Section II.B.

$$L_{tank_{\forall}} = L_{pay} - \left[(L_{bus} + L_{dock})n_{dock} + \left(L_{thrust} + L_{eng}\right)B_{eng}\right] \quad \text{Eq. 45}$$

The length of the cylindrical section of the tank L_{cyl} is based on L_{tank} (generic length, it does not matter if its volume or mass limited) with $2h_{dome}$ subtracted from it as shown in Eq. 46.

The surface area and volume of the cylindrical section ($A_{s_{cyl}}$ and $\forall_{cyl}$) use the standard cylindrical geometrical equations shown in Eq. 47 and Eq. 48, respectively. The resulting total surface area and volume of the tank ($A_{s_{tank}}$ and $\forall_{tank}$) consist of two domes and the cylinder as shown in Eq. 49 and Eq. 50, respectively.

$$L_{cyl} = L_{tank} - 2h_{dome} \qquad \text{Eq. 46}$$

$$A_{s_{cyl}} = 2\pi r_{tank} L_{cyl} \qquad \text{Eq. 47}$$

$$\forall_{cyl} = \pi r_{tank}^2 L_{cyl} \qquad \text{Eq. 48}$$

$$A_{s_{tank}} = A_{s_{cyl}} + 2A_{s_{dome}} \qquad \text{Eq. 49}$$

$$\forall_{tank} = \forall_{cyl} + 2\forall_{dome} \qquad \text{Eq. 50}$$

The total propellant mass inside the tank m_{prop} is based on $\forall_{tank}$ and propellant density ρ_{prop} as shown in Eq. 51. The usable propellant mass $m_{prop_{use}}$ accounts for the ullage δ_U (units in percent) and the resulting formulation shown in Eq. 52.

$$m_{prop} = \forall_{tank} \rho_{prop} \qquad \text{Eq. 51}$$

$$m_{prop_{use}} = m_{prop}\left(1 - \frac{\delta_U}{100}\right) \qquad \text{Eq. 52}$$

To find the mass of the tank m_{tank}, the thickness of the tank t_{tank} needs to be evaluated which is based on the internal pressure of the tank P_{prop} and the static hydraulic pressure P_{hyd} caused by the launch vehicle acceleration which is characterized by the axial loads G_{axial}. is determined by Eq. 53 where g is 9.807 m/s^2 and the maximum pressure of the tank P_{max} that will be used in determining the tank thickness is shown in Eq. 54. It is assumed that the tank is an isogrid structure and the thickness of the isogrid skin t_{skin} is provided by Eq. 55 which is based on P_{max}, a factor of safety FS, r_{tank}. yield strength of the material σ_Y, the first non-dimensional iso-grid geometry property α, and the knockdown parameter k which accounts for the added tension in bending from lateral loads. The equivalent weight thickness $\bar{t}$ is provided by Eq. 56 which provides the thickness of a non-iso-grid tank with the same size and mass as an iso-grid tank and is based on t_{skin}, α, and a second non-dimensional isogrid geometrical property μ which is 0 for an unflanged iso-grid. The dome thickness $\bar{t}_{dome}$ is obtained by scaling $\bar{t}$ by a thickness ratio T_R as shown in Eq. 57. The dry mass of the tank $m_{tank_{dry}}$ is found by scaling the surface areas of the cylindrical $A_{s_{cyl}}$ and dome $A_{s_{dome}}$ components of the tank by their respective thicknesses $\bar{t}$ and $\bar{t}_{dome}$ to obtain the volume of the material $\forall_{mat}$ and scaling it by the material density ρ_{mat} as shown in Eq. 58. m_{tank} includes $m_{tank_{dry}}$ and m_{prop} as shown in Eq. 59.

$$P_{hyd} = L_{tank} \rho_{prop} g G_{axial} \qquad \text{Eq. 53}$$

$$P_{max} = P_{prop} + P_{hyd} \qquad \text{Eq. 54}$$

$$t_{skin} = \frac{P_{max} r_{tank} FS}{2\sigma_Y k(1+\alpha)} \qquad \text{Eq. 55}$$

$$\bar{t} = t_{skin}[1 + 3(\alpha + \mu)] \qquad \text{Eq. 56}$$

$$\bar{t}_{dome} = \bar{t}T_R \quad \text{Eq. 57}$$

$$m_{tank_{dry}} = \rho_{mat}\left(A_{s_{cyl}}\bar{t} + 2A_{s_{dome}}\bar{t}_{dome}\right) \quad \text{Eq. 58}$$

$$m_{tank} = m_{tank_{dry}} m_{prop} \quad \text{Eq. 59}$$

II.A.8 Power Management and Distribution (PMAD)

The Power Management and Distribution (PMAD) module depends on the peak power draw $\dot{W}_{peak}$ and outputs the PMAD mass m_{PMAD}, required power $\dot{W}_{req}$, and waste heat $\dot{Q}_{waste}$. The box and cable specific masses, $m_{sp_{box}}$ and $m_{sp_{cable}}$, respectively, are determined by scaling a user defined normalized box mass $\bar{m}_{box}$ and normalized cable mass $\bar{m}_{cable}$ by 0.0105 kg/W as shown in Eq. 60 and Eq. 61, respectively. The box mass per PMAD unit m_{box} is determined from $\dot{W}_{peak}$ and $m_{sp_{box}}$ as shown in Eq. 62. Similarly, the cable mass per PMAD unit m_{cable} is dependent on $\dot{W}_{peak}$ and $m_{sp_{cable}}$ as shown in Eq. 63. The total PMAD mass m_{PMAD} is then the summation of m_{box} and m_{cable} and is scaled by the number of PMAD units n_{PMAD} as shown in Eq. 64. The required power $\dot{W}_{req}$ is dependent on the PMAD efficiency η_{PMAD} and $\dot{W}_{peak}$ as shown in Eq. 65. The waste heat $\dot{Q}_{waste}$ is then the difference between $\dot{W}_{req}$ and $\dot{W}_{peak}$ as shown in Eq. 66.

$$m_{sp_{box}} = 0.0105\bar{m}_{box} \quad \text{Eq. 60}$$

$$m_{sp_{cable}} = 0.0105\bar{m}_{cable} \quad \text{Eq. 61}$$

$$m_{box} = \dot{W}_{peak} m_{sp_{box}} \quad \text{Eq. 62}$$

$$m_{cable} = \dot{W}_{peak} m_{sp_{cable}} \quad \text{Eq. 63}$$

$$m_{PMAD} = (m_{box} + m_{cable})n_{PMAD} \quad \text{Eq. 64}$$

$$\dot{W}_{req} = \frac{\dot{W}_{peak}}{\eta_{PMAD}} \quad \text{Eq. 65}$$

$$\dot{Q}_{waste} = \dot{W}_{req} - \dot{W}_{peak} \quad \text{Eq. 66}$$

II.A.9 Radiator and Mechanisms

The radiator depends on the CFM heat rejection $\dot{Q}_{CFM}$ and the waste heat from the PMAD $\dot{Q}_{PMAD_{waste}}$, and it outputs the mass of the radiator panels m_{rad} and the mass of the radiator mechanisms $m_{rad_{mech}}$. A user specified parameter is defined that provides information about if the radiator radiates from only one side or both sides and is used in the calculations as an area modifier A_M of 0.5 for both sides and 1 for a single side. The area of the radiator A_{rad} is determined by the radiative heat transfer equation that is dependent on $\dot{Q}_{CFM}$ and $\dot{Q}_{PMAD_{waste}}$, a factor of safety FS, Stefan-Boltzmann constant of $\sigma = 5.67 \times 10^{-8}$, radiator emissivity ε, radiator temperature that is user specified T_{rad} (future iterations of this module will include a more detailed radiator analysis to remove this assumption), the environmental temperature T_{env} that is typically assumed to be between 3 K and 4 K, and A_M as shown in Eq. 67. The mass of the radiator panels m_{rad} is determined by a radiator areal density ρ_{rad} and A_{rad} as shown in Eq. 68. To obtain the mass of the radiator mechanisms $m_{rad_{mech}}$, A_{rad} is scaled by 3.4 as shown in Eq. 69.

$$A_{rad} = \frac{\left(\dot{Q}_{CFM} + \dot{Q}_{PMAD_{waste}}\right)FS}{\sigma\varepsilon(T_{rad}^4 - T_{env}^4)} A_M \qquad \text{Eq. 67}$$

$$m_{rad} = \rho_{rad} A_{rad} \qquad \text{Eq. 68}$$

$$m_{rad_{mech}} = 3.4 A_{rad} \qquad \text{Eq. 69}$$

II.A.10 Reaction Control System (RCS)

The Reaction Control System (RCS) module determines the total RCS mass m_{RCS}, wetted mass $m_{RCS_{wet}}$, piping mass $m_{RCS_{pipe}}$, mass of thrusters $m_{RCS_{thrusters}}$, power of thrusters $\dot{W}_{RCS_{thrusters}}$, power for the piping $\dot{W}_{RCS_{pipe}}$, dry mass of the RCS system $m_{RCS_{dry}}$, and the RCS propellant mass $m_{RCS_{prop}}$ given the required RCS ΔV_{RCS} and the mass of the spacecraft m_{SC}. $m_{RCS_{prop}}$ is determined based on the Ideal Rocket Equation, m_{SC}, RCS specific impulse $I_{sp_{RCS}}$, g, and the tank ullage δ_U as shown in Eq. 70. A mixture mass ratio ϕ is used to determine the mass of the fuel m_{fuel} and the mass of the oxidizer m_{ox} as shown in Eq. 71 and Eq. 72, respectively. At this point, the calculations split between the fuel and oxidizer, however, they are the same for each fluid.

$$m_{RCS_{prop}} = \left[m_{SC} \exp\left(\frac{\Delta V_{RCS}}{I_{sp_{RCS}} g}\right)\right](1 + \delta_U) \qquad \text{Eq. 70}$$

$$m_{fuel} = \frac{m_{RCS_{prop}}}{1 + \phi} \qquad \text{Eq. 71}$$

$$m_{ox} = m_{RCS_{prop}} - m_{fuel} \qquad \text{Eq. 72}$$

The mass of fluid per tank $m_{fluid_{tank}}$ is determined by the total mass of the fluid m_{fluid} (m_{fuel} or m_{ox}) and the total number of RCS tanks $n_{RCS_{tank}}$ which include both fuel and oxidizer tanks as shown in Eq. 73. The internal volume of the tank $\forall_{in}$ is determined by $m_{fluid_{tank}}$, density of the fluid ρ_{fluid}, and δ_U as shown in Eq. 74. Assuming that the tank is a spherical shape, the internal radius of the tank r_{in} is determined by $\forall_{in}$ as shown in Eq. 75. The maximum pressure that the tank experiences P_{max} is due the tank stagnation pressure P_0 and axial loads G_{axial} which depend on r_{in} and ρ_{fluid} as shown in Eq. 76. The designed burst pressure P_{burst} is based on a factor of safety FS and P_{max} as shown in Eq. 77. The thickness of the tank walls $t_{tank_{RCS}}$ is determined by P_{burst}, r_{in}, yield strength of the material σ_Y, and FS as shown in Eq. 78. The external volume of the tank $\forall_{ex}$ is dependent on r_{in} and $t_{tank_{RCS}}$ as shown in Eq. 79. The dry mass of each tank $m_{tank_{dry_{fluid}}}$ is based on both $\forall_{in}$ and $\forall_{ex}$ as well as the density of the material of the tank $\rho_{mat_{RCS}}$ as shown in Eq. 80. The wetted mass of each tank $m_{tank_{wet_{fluid}}}$ is the summation of $m_{tank_{dry_{fluid}}}$ and $m_{fluid_{tank}}$ as shown in Eq. 81.

$$m_{fluid_{tank}} = \frac{2 m_{fluid}}{n_{RCS_{tank}}} \qquad \text{Eq. 73}$$

$$\forall_{in} = \frac{m_{fluid_{tank}}}{\rho_{fluid}(1 - \delta_U)} \qquad \text{Eq. 74}$$

$$r_{in} = \left(\frac{3\forall_{in}}{4\pi}\right)^{1/3} \quad \text{Eq. 75}$$

$$P_{max} = P_0 + \rho_{fluid} r_{in} G_{axial} g \quad \text{Eq. 76}$$

$$P_{burst} = P_{max} FS \quad \text{Eq. 77}$$

$$t_{tank_{RCS}} = \frac{P_{burst} r_{in} FS}{\sigma_Y} \quad \text{Eq. 78}$$

$$\forall_{ex} = \frac{4}{3}\pi\left(r_{in} + t_{tank_{RCS}}\right)^3 \quad \text{Eq. 79}$$

$$m_{tank_{dry_{fluid}}} = (\forall_{ex} - \forall_{in})\rho_{mat_{RCS}} \quad \text{Eq. 80}$$

$$m_{tank_{wet_{fluid}}} = m_{tank_{dry_{fluid}}} + m_{fluid_{tank}} \quad \text{Eq. 81}$$

The total volume $\forall_{tot}$ is the summation of the volumes of the fuel $\forall_{fuel}$ and oxidizer $\forall_{ox}$ with the number of tanks allocated for each accounted as shown in Eq. 82. The mass of the helium pressurization system m_{He} is determined by scaling the summation of the dry tank mass of the fuel $m_{tank_{dry_{fuel}}}$ and the dry tank mass of the oxidizer sc system m_{RCS} is the summation of the wetted mass of the tanks $m_{RCS_{wet}}$, $m_{RCS_{pipe}}$, and thrusters $m_{RCS_{thrusters}}$ as shown in Eq. 88.

$$\forall_{tot} = \frac{n_{RCS_{tank}}}{2}\left(\forall_{fuel} + \forall_{ox}\right) \quad \text{Eq. 82}$$

$$m_{He} = 0.179279 \frac{n_{RCS_{tank}}}{2}\left(m_{tank_{dry_{fuel}}} + m_{tank_{dry_{ox}}}\right) \quad \text{Eq. 83}$$

$$\begin{aligned} m_{RCS_{dry}} &= \frac{n_{RCS_{tank}}}{2}\left(m_{tank_{dry_{fuel}}} + m_{tank_{dry_{ox}}}\right) + m_{He} \\ &= 1.179279 \frac{n_{RCS_{tank}}}{2}\left(m_{tank_{dry_{fuel}}} + m_{tank_{dry_{ox}}}\right) \end{aligned} \quad \text{Eq. 84}$$

$$m_{RCS_{wet}} = \frac{n_{RCS_{tank}}}{2}\left(m_{tank_{wet_{fuel}}} + m_{tank_{wet_{ox}}}\right) + m_{He} \quad \text{Eq. 85}$$

$$m_{RCS_{pipe}} = 0.02 m_{RCS_{wet}} \quad \text{Eq. 86}$$

$$m_{RCS_{thrusters}} = m_{RCS_{thruster}} n_{thrusters} \quad \text{Eq. 87}$$

$$m_{RCS} = m_{RCS_{wet}} + m_{RCS_{pipe}} + m_{RCS_{thrusters}} \quad \text{Eq. 88}$$

The power of the thrusters $\dot{W}_{RCS_{thrusters}}$ and piping $\dot{W}_{RCS_{pipe}}$ is determined by scaling the power of each thruster $\dot{w}_{RCS_{thruster}}$ and pipe $\dot{w}_{RCS_{pipe}}$ by $n_{thrusters}$ as shown in Eq. 89 and Eq. 90, respectively.

$$\dot{W}_{RCS_{thrusters}} = \dot{w}_{RCS_{thruster}} n_{thrusters} \quad \text{Eq. 89}$$

$$\dot{W}_{RCS_{pipe}} = \dot{w}_{RCS_{pipe}} n_{thrusters} \quad \text{Eq. 90}$$

II.A.11 Solar Arrays

The solar array module has the required power to the loads during the daytime $\dot{W}_{req_{day}}$ as a single input. The outputs of this module are the masses of the array m_{array} and the mechanical components m_{mech}. It is assumed that the power required during the day for the loads is the same power required during the night as shown in Eq. (1). However, further work could show that additional power would be required during the night for heating the electrical components unless the heat rejected from CFM could be redirected to supply the required heat. The required power for the arrays $\dot{W}_{array}$ is based on the required power levels to the loads, the amount of time the spacecraft spends during the day T_d and during the night T_n, and the efficiencies of the power going through the batteries to the loads X_e and the power going to the loads directly while bypassing the batteries X_d as shown in Eq. (2). The mass of the array m_{array} is determined by the specific mass $m_{sp_{array}}$, $\dot{W}_{array}$, and the array mass margin M_{array} (in percent) as shown in Eq. (3). The masses of the other components such as the gimbal, release mechanism, and harness are determined using Eq. (4). Here, m_{tot_i} is the total mass of component i, m_i is the mass of a single component i, n_i is the number of i components, and M_i is the mass margin of component X. Using this, the total mass of the mechanical components is defined in Eq. (5) where k is the total number of the types of components.

$$\dot{W}_{req_{day}} = \dot{W}_{req_{night}} = \dot{W}_{req} \qquad \text{Eq. 91}$$

$$\dot{W}_{array} = \frac{1}{T_d}\left(\dot{W}_{req_{day}}\frac{T_d}{X_d} + \dot{W}_{req_{night}}\frac{T_e}{X_e}\right) \qquad \text{Eq. 92}$$

$$m_{array} = m_{sp_{array}}\dot{W}_{array}\left(1 + \frac{M_{array}}{100}\right) \qquad \text{Eq. 93}$$

$$m_{tot_i} = m_i n_i\left(1 + \frac{M_i}{100}\right) \qquad \text{Eq. 94}$$

$$m_{mech} = \sum_{i=1}^{k} m_{tot_i} = \sum_{i=1}^{k} m_i n_i\left(1 + \frac{M_i}{100}\right) \qquad \text{Eq. 95}$$

II.B. Master Equipment List Integration

The master equipment list integration module combines the physics models of Section II.A and provides the spacecraft propellant mass, RCS propellant mass, structural mass, and propellant volume. The constants and specifications that are set for the physics models are read as a first step to this model which include over 100 parameters. The reader is advised to contact the lead author for more information on these values. The spacecraft mass, peak power draw, and mass limited payload length are guessed with arbitrary values to start the calculations due to interdependencies. The order that the physics models are executed are as follows: Bus Structure, Docking Structure, Engine, Thrust Structure, Communications/Command & Data-Handling Systems/Guidance, Navigation, & Control, Main Propellant Tank, Reaction Control System, Cryogenic Fluid Management, Power Management and Distribution, and Solar Arrays. At this point, all the modules except for the Battery have been executed. The peak power draw is determined by the summation of all the power draws resulting from the outputs from all the executed physics modules and inputted into the Battery module. The mass of all the components is then summed and compared to that of the previous iteration. This repeats until convergence of the spacecraft mass.

II.C. RCS and OMS Burns

The Architecture model will read the Vehicle Card and iterate through all the burns listed on it. Both RCS and OMS burns use the Ideal Rocket Equation to determine the propellant mass used to achieve the desired ΔV as shown in Eq. 94.

$$m_{prop\,used} = \left(m_{dry} + m_{RCS} + m_{prop}\right)\left[1 - \exp\left(-\frac{\Delta V}{I_{sp}}\right)\right] \qquad \text{Eq. 94}$$

II.D. NTP Burns

II.D.1 Decay Heating

The NTP burns use the quasi-steady-state database from a specified engine to perform transient burns with the incorporation of point kinetics and decay heating using Eq. 95 with the constant parameters specified in Table 2 taken from BWXT's analysis. The resulting $Q_{decay} = \int_{t_{fp}}^{t_{sd}} \dot{Q}_{decay}(t)dt$ value is used in determining the required $m_{cooldown}$ and thus the $\Delta V_{cooldown}$ if a cooldown specific impulse $I_{sp_{cooldown}}$ is assumed. For H-NTP, A-NTP, and M-NTP these values are 500 sec, 250 sec, and 200 sec, respectively [3,8,9].

$$\begin{aligned}\dot{Q}_{decay}(t) = \dot{Q}_{avg}\Bigg\{&\frac{\rho}{\rho-\beta}\exp\left(\frac{\rho-\beta}{\Lambda}t\right) - \frac{\beta}{\rho-\beta}\exp\left(\frac{-\rho\lambda}{\rho-\beta}t\right) \\ &+ 0.1104\left[t^{-0.2436} - \left(t_{fp}+t\right)^{-0.2436}\right]\Bigg\}\end{aligned} \qquad \text{Eq. 95}$$

Table 2: Neutronics Constants

Constant	Symbol	Given Values	
Fission Yield	β	0.0065	--
Decay Constant	λ	0.0764	s^{-1}
Prompt Neutron Lifetime	Λ	6×10^{-5}	s
Reactivity	ρ	-0.01377	$

II.D.2 NTP Engine Transients

A ramp limit is set by a temporal derivative which used to evaluate the quasi-steady-state database with reactor power $\frac{\mathrm{d}\dot{Q}}{\mathrm{dt}}$ and fuel temperature $\frac{\mathrm{d}T_f}{\mathrm{dt}}$ being those with the most interest. Based on the temporal derivative $\frac{dX}{dt}$ criteria, the engine transient performance is evaluated. It is important to note that all parameters in the quasi-steady-state database are functions of $\dot{Q}$. In any case, the transient calculation starts from power level of the previous iteration $\dot{Q}_{i-1}$ and aims to obtain a desired power level $\dot{Q}_{des}$. For powering up, $\dot{Q}_{des}$ is set to the reactor full power and for powering down, $\dot{Q}_{des}$ is set to the idle power level which is 7 kWt from SNP specifications where the residual reactor heat can be dissipated through radiation alone. From the $\frac{dX}{dt}$ criteria, the parameter X that is to be ramped at iteration i, or X_i, is evaluated at $\dot{Q}_{i-1}$ and at $\dot{Q}_{des}$ to yield X_{i-1} and X_{des}, respectively. The $\frac{dX}{dt}\Delta t$ is added to X_{i-1} to yield X_i. Should X_i evaluate to a value that is beyond X_{des}, then X_i is set to be equal to X_{des}. This provides a constant ramp rate for X from which $\dot{Q}_i$ is obtained. Since decay heating is considered, Eq. 3.5 is evaluated and $\dot{Q}_{decay}$ is added to $\dot{Q}_i$ such that $\dot{Q}_i = \dot{Q}_i + \dot{Q}_{decay}$. Based on the new $\dot{Q}_i$, all other parameters are evaluated using makima interpolation of the quasi-steady-state parameters. At each iteration, the burn time t is incrementally increased by Δt and the evaluated parameters at each iteration are recorded in an array which includes the engine thrust F and mass flow rate $\dot{m}$.

II.D.3. Vehicle Performance

During each iteration, the propellant mass m_{prop_i} is calculated by subtracting $\dot{m}\Delta t$ from $m_{prop_{i-1}}$. The total vehicle mass is calculated by $m_{tot_i} = m_{prop_i} + m_{RCS} + m_{dry}$. Furthermore, ΔV_i is calculated from the average total vehicle mass between iterations $i-1$ and i by $\overline{m}_{tot_i} = \frac{m_{tot_{i-1}} + m_{tot_i}}{2}$ and applying the thrust of all the engines $n_{engines}F$ on the engine block through Newton's second law or $\Delta V_i = \Delta V_{i-1} + \frac{n_{engines}F}{\overline{m}_{tot_i}}$. This method could be used to either calculate the total ΔV capability of a defined vehicle or to converge to a ΔV by changing the vehicle's propellant volume and thereby the corresponding dry masses of the MEL by rerunning the calculations described in Section II.

III. 1st GENERATION NTP ENGINE FLIGHT TEST MATRIX

A similar study on Operational Cis-Lunar Missions was conducted which is now known as 2nd Generation NTP missions [10] and the same can be applied for the 1st Generation NTP demonstration mission classes and vehicle configurations as shown in Table 3. Here, no payload mass is considered for any of these mission classes given that this is fundamentally a flight test. Therefore, the engine itself could be viewed as the payload. This matrix aims to explore various propellant options, engine architectures, and mission scopes. The goal of each case is to fit everything on a single commercial launch vehicle, which is why the SLS launch vehicle variants are not included. Each class/configuration also assumes that 100 m/s of ΔV is used before the burn(s) is/are performed which affects the total capability of an option in the matrix. Cryogenic fluid management is used and sized for hydrogen and methane. Accordingly, the launch vehicle payload sizes and capabilities, shown in Table 4, will significantly impact the performance of the configured vehicle. Each vehicle configuration is to be launched into a nuclear safe 1000 km X 1000 km circular orbit [11] which is reflected in the payload capability of each launch vehicle in Table 4. The ΔV achieved per burn accounts for the startup, steady state, shutdown, and cooldown ΔVs. Using this ΔV and the total propellant mass expelled during the entire burn and cooldown, the average specific impulse is calculated via Ideal Rocket Equation. The Missions Classes that are considered are those that produce either 1 km/s or 2.5 km/s lumped together as X ΔV Mission Classes and those that attempt to use all of the available launch vehicle payload mass or payload bay volume limitations, which ever limitation is most limiting, lumped togerher as X-Burn Mission Classes.

Table 3: 1st Generation NTP Trade Matrix

Thrust-Engine Mass	Propellant-Isp	Launch Vehicles	Mission Class/# Burns (*equally distributed ΔV*)
10klbf-3000kg	H-750	Starship	1 (limit to 1 km/s)
12.5klbf-3400kg	H-825	New Glenn	1 (limit to 2.5 km/s)
15klbf-3400kg	H-900	Falcon 9 Recoverable	2 (max LV ΔV)
25klbf-3400kg (ammonia)	A-375	Falcon Heavy Recoverable	4 (max LV ΔV)
25klbf-5000kg	A-450	Vulcan	
	M-350		
	M-494		

Table 4: Considered Launch Vehicles and Their Capabilities

Parameter	Falcon Heavy Recoverable	Falcon 9 Recoverable	Vulcan	New Glenn	Starship
Payload to 1000km X 1000km Orbit (kg)	18000.0	16800.0	18450.0	31550.0	109240.0
Fairing diameter (m)	5.2	5.2	5.4	7.0	9.0
Fairing length (m)	18.6	18.6	21.3	19.6	18.0
Payload diameter (m)	4.6	4.6	4.8	6.4	8.0
Payload length (m)	16.5	16.5	18.6	18.5	17.2
Volume (m^3)	240.0	240.0	280.0	487.0	650.0

IV. RESULTS AND DISCUSSION

The matrix outlined in Section III was evaluated using the MEL methodology discussed in Section II along with the accompanying quasi-steady-state engine datasets analyzed through the X-NTP model. Given the breadth of different vehicle configurations, the results will be presented for each Mission Class to analyze the performance of each configuration given a single convergence criterion. The spread of each propellant along the plots results from varying the thermal performance of the engine that leads to the variation of the specific impulse, varying the engine thrust and correspondingly the engine mass, and varying the different launch vehicles. The spread of the specific impulse values per propellant type per thermal engine performance are caused by the different burn times affected by the transients. These effects were described in detail via prior work [5]. These variations were separated to provide a more complete view of the interdependency of each parameter. Afterwards, a dimensionless analysis will be performed to develop tools to form a flight test based on user defined requirements and utility.

IV.A. 1st Generation NTP Missions Matrix

The X km/s Mission Classes converge by adjusting the propellant mass to meet a specific ΔV requirement while still maintaining the 100 m/s ΔV imposed on the RCS system. Figure 1 shows the 1 km/s Mission Class with a single burn. This is the least demanding of all considered missions for all configurations. Here, the propellant mass for each engine thrust class increases which corresponds to the increase in dry mass. Given that the payload diameter is significantly higher for the New Glenn and Starship launch vehicles when compared to the Falcon series and Vulcan vehicles, the propellant mass is accordingly higher which is also reflected in the dry mass. Therefore, the 5000 kg NTP engines onboard the New Glenn and Starship vehicles yield the largest dry mass of all considered cases for this mission class. Lower thrust levels also result in higher burn times which could be beneficial from the point of view of a flight test to provide more data for the test operators. However, the increased burn time will also be strenuous on the reactor, particularly, the fuel elements. Each considered propellant has a unique specific impulse with the bounding case of M-NTP having the largest range in propellant mass distribution due to its pyrolysis mechanics. For the 1 km/s mission class, A-NTP can provide the lowest dry mass and the lowest burn times. Therefore, in terms of developmental risk for this Mission Class, A-NTP will offer the lowest risk given that no cryocooler development will be necessary and the reactor materials will not be required to withstand high temperatures for as long as other propellants. However, the objective of testing with hydrogen will be lost and the vehicle mass to be launched will be double that of H-NTP.

For this Mission Class, given that M-NTP will still require cryocoolers, if the pyrolysis mechanics allow these engines to produce the optimistic 494 second specific impulse, then they will perform similarly to A-NTP in terms of propellant mass and some of the burn times, but still carry the mass penalty of cryocoolers. However, if pyrolysis mechanics, or lack thereof, yield pure methane coming out of the nozzle, then only allow M-NTP to produce 350 seconds of specific impulse, then these engines will have the most propellant mass and longest burn times accordingly.

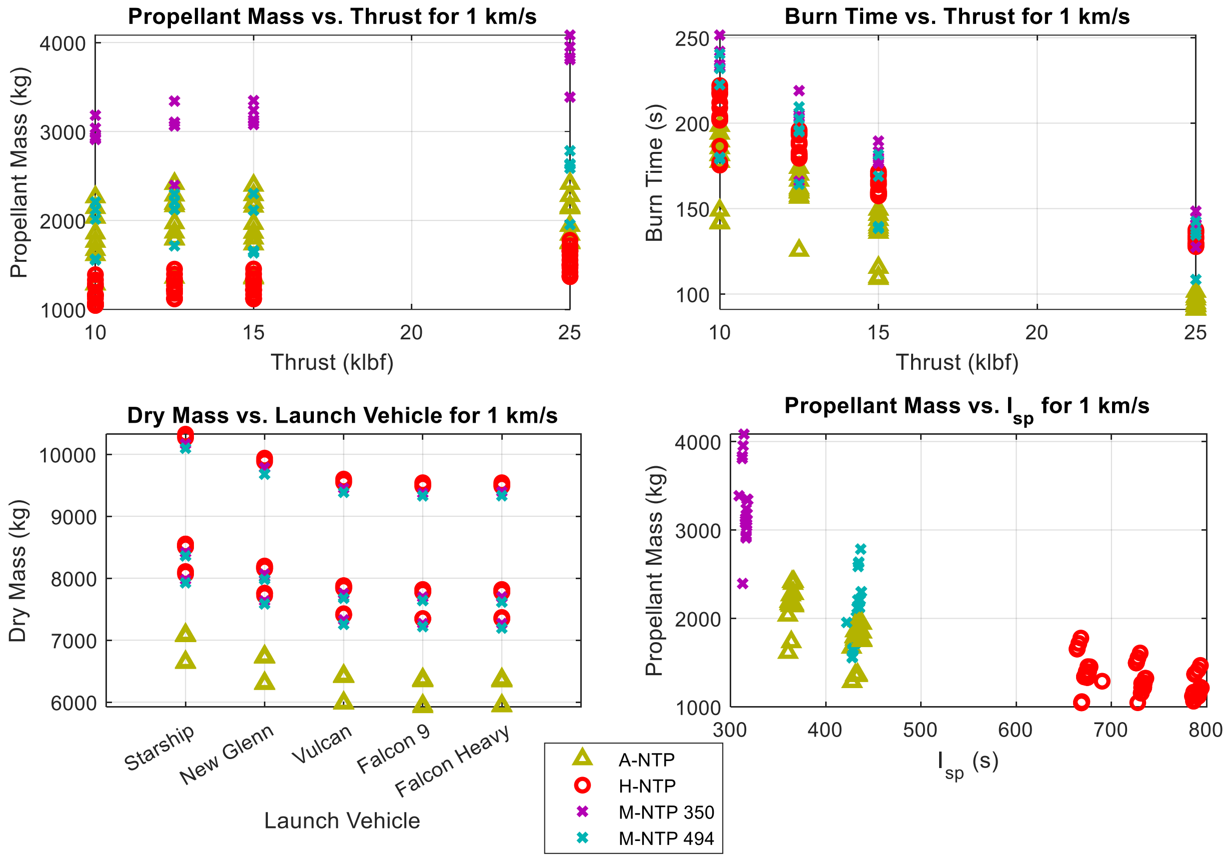

Figure 1: Parameters for 1 km/s Mission Class (Top Left: Propellant Mass vs. Thrust, Top Right: Burn Time vs. Thrust, Bottom Left: Dry Mass vs. Launch Vehicle, and Bottom Right: Propellant Mass vs. Specific Impulse)

The next Mission Class that was analyzed is the 2.5 km/s of ΔV performed by a single burn with its parameters shown in Figure 2. Much like the 1 km/s mission class, the trends are the same except that the values themselves are larger, including the burn time, which makes the data points appear to be more clustered together. Furthermore, A-NTP also appears to be slightly less attractive in terms of dry mass when the Starship or New Glenn launch vehicles are utilized. H-NTP has a much lower propellant mass than both A-NTP and M-NTP given its significantly higher specific impulse. Both A-NTP and M-NTP also appear to be performing closer together in terms of propellant mass with A-NTP performing similarly to the higher specific impulse M-NTP variant. Again, the Starship launch vehicle has the highest dry mass due to the larger payload diameter followed by New Glenn and then by the rest of the launch vehicles. In both 1 km/s and 2.5 km/s Mission Classes, the higher engine thrust and corresponding higher engine mass is correlated with both shorter burn times and more propellant mass across the same specific impulse and propellant selections.

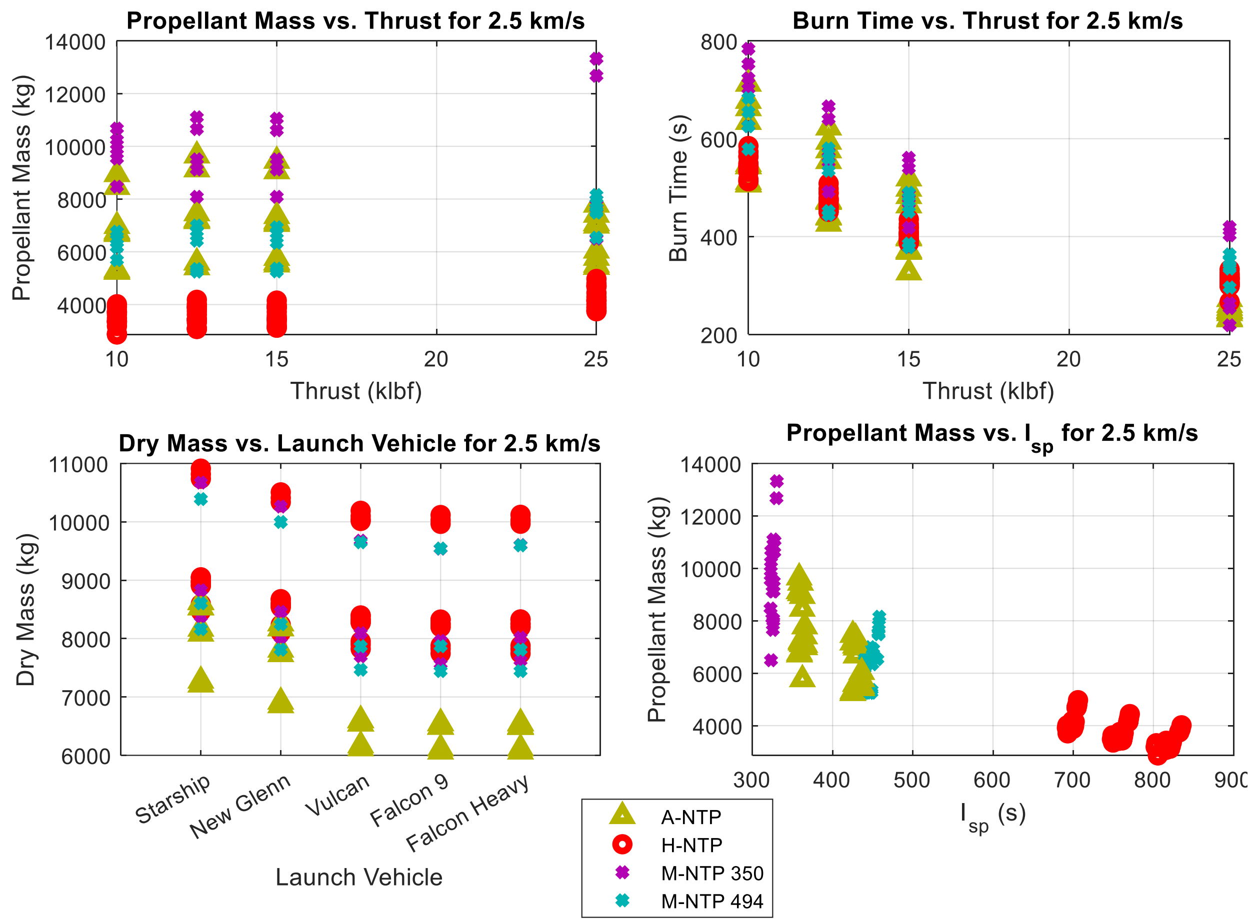

Figure 2: Parameters for 2.5 km/s Mission Class (Top Left: Propellant Mass vs. Thrust, Top Right: Burn Time vs. Thrust, Bottom Left: Dry Mass vs. Launch Vehicle, and Bottom Right: Propellant Mass vs. Specific Impulse)

The X-Burn Mission Classes switch the convergence criteria from adjusting the propellant mass to meet a ΔV requirement to determining the maximum ΔV that could be performed by exhausting the launch vehicle capabilities and still maintaining the 100 m/s ΔV requirement imposed on the RCS. Furthermore, the ΔV achieved is split equally between the burns. For both the 2-Burn and 4-Burn Mission Classes shown in Figure 3 and Figure 4, respectively, the volume limitation of hydrogen is highlighted and is primarily exaggerated in the case of the Starship launch vehicle where both A-NTP and M-NTP configured vehicles have propellant masses of around 90 mton while the H-NTP configurated vehicles have a maximum propellant mass of around 36 mton. The same dry mass trends exist in the X-Burn Mission Classes as they do in the X km/s Mission Class. According to the engine thrust class, lower thrust levels are able to achieve longer burn times with the same benefits as mensioned in the X km/s Mission classes in terms of flight testing. Both A-NTP and M-NTP can provide either the longest or shortest burn time depending on the launch vehicle selected with H-NTP performing in between the two. Given H-NTP's high specific impulse, higher ΔVs can be achieved with lower propellant mass. However, given that both H-NTP and M-NTP require cryocoolers and are less dense than ammonia, these two vehicle configurations require the highest dry mass. To achieve similar ΔV values as H-NTP, both A-NTP and M-NTP need roughly three times the propellant mass. If the Starship launch vehicle is considered, all propulsion system variants can provide similar ΔV values between 6 km/s and 10 km/s as the systems are either volume or mass limited. For the smaller launch vehicles, H-NTP provides a higher ΔV. These trends are the same for both 2-Burn and 4-Burn Mission Classes with the 4-Burn Mission Class having a slightly lower overall ΔV across all vehicle configurations due to more propellant mass used during cooldown with a lower specific impulse value given twice as many burns.

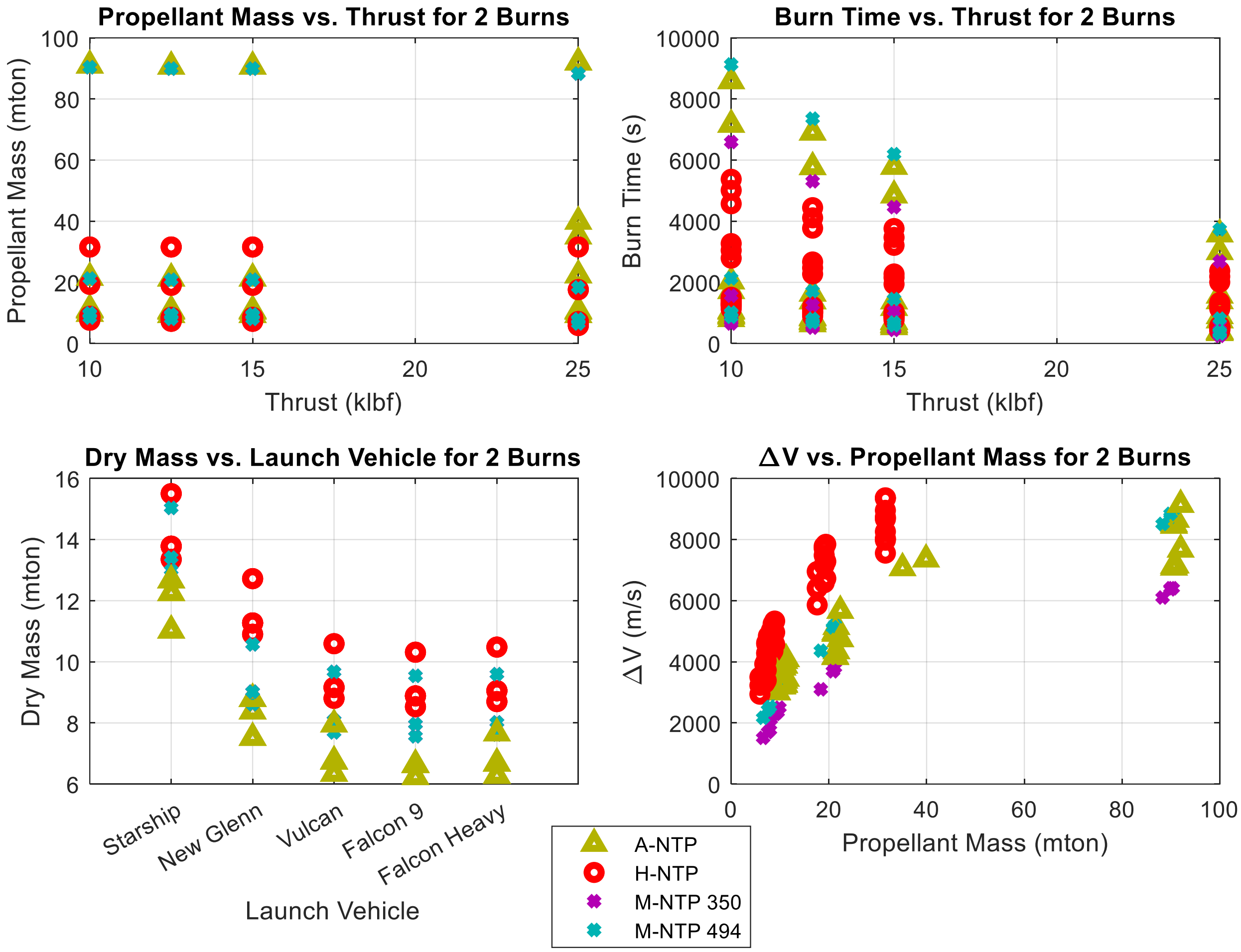

Figure 3: Parameters for a 2-Burn Mission Class (Top Left: Propellant Mass vs. Thrust, Top Right: Burn Time vs. Thrust, Bottom Left: Dry Mass vs. Launch Vehicle, and Bottom Right: ΔV vs. Propellant Mass)

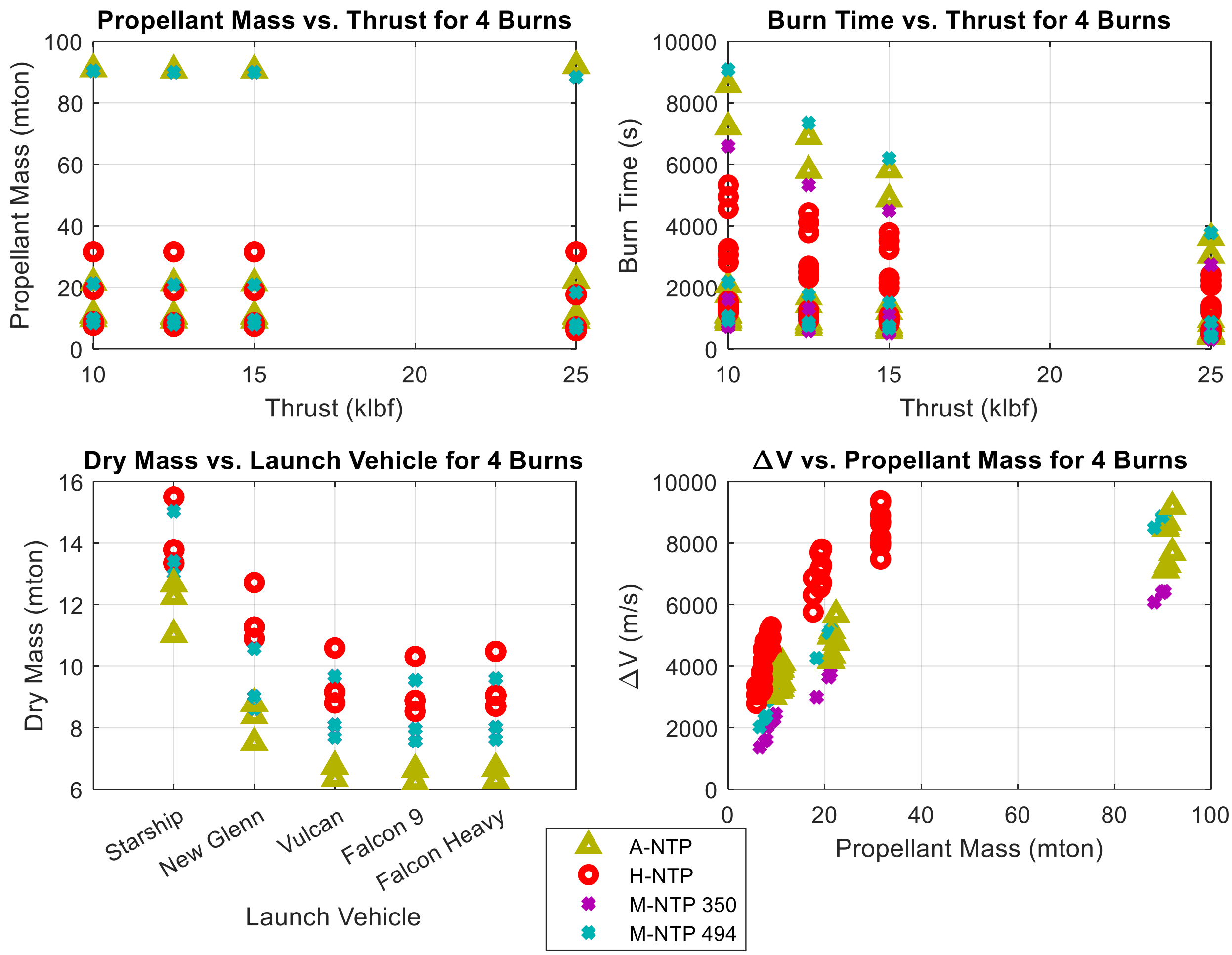

Figure 4: Parameters for a 4-Burn Mission Class (Top Left: Propellant Mass vs. Thrust, Top Right: Burn Time vs. Thrust, Bottom Left: Dry Mass vs. Launch Vehicle, and Bottom Right: ΔV vs. Propellant Mass)

A conclusion from this analysis that could be made is regarding the heavier launch vehicles such as Starship and New Glenn. These vehicles are advantageous in terms of mission capability such as ΔV, but not necessarily in terms of dry mass. Longer burn times could be preferable from a testing standpoint given that there would be more time to gather data and perhaps even expand beyond the initial mission objective. From this point of view, the Starship launched M-NTP or A-NTP 10 klbf configured vehicles would provide the most utility followed closely by H-NTP.

IV.B. Dimensionless Analysis

Dimensionless parameters are a useful tool to characterize complex datasets by either using fractional equivalents such as the case of the mass ratio MR in the Ideal Rocket Equation or a dimensionless parameter that reduces the complexity of a system into smaller, meaningful, non-dimensional groups using the Buckingham Π theorem. The following analysis presents results that are independent of the number of burns, propellant type, and launch vehicle. The analysis will guide the design engineer in choosing the propellant type based on the specific impulse and the launch vehicle based on the desired ΔV. As was shown previously, the parameter that describes the number of burns does not play a significant role in the vehicle configuration.

IV.B.1 Formation of Dimensionless Parameters

For the dataset presented in the current analysis, the specific impulse and the burn duration are combined into a ratio $\frac{I_{sp}}{t_{burn}}$. This ratio can be conceptually described as the mass efficiency of the vehicle, with larger values representing high propellant usage effectiveness and lower values representing low propellant usage effectiveness. This differs from using only the the specific impulse, as the amount of propellant onboard the vehicle is directly translated into the burn time given the specific impulse. Using the burn time directly with the specific impulse eliminates consideration of the propellant mass, which is useful in terms of this flight test where longer burn times may be more preferable, resulting in a preferably lower $\frac{I_{sp}}{t_{burn}}$ value. On the other hand, the mass ratio takes into account the inert mass divided by the total initial mass which results in higher values being more efficient from a propellant mass perspective. When MR is plotted as a function of $\frac{I_{sp}}{t_{burn}}$ for all Mission Class and vehicle configurations as shown in Figure 5, all of the values fall on a trend. This trend has a "knee in the curve" at a $\frac{I_{sp}}{t_{burn}}$ value of 1 which corresponds to a MR of 0.6. Furthermore, Eq. 96 provides the fit relationship as described by function f_1 with $\pm 10\%$ bounds encompassing the majority of the cases which could be used as a tool to engineer a particular mission and determine where it would fall on the plot. Finally, there are areas where a particular propellant is denser and other areas where all propellants are comparable which provides the mission designer insight as to which propulsion system would meet the imposed requirements.

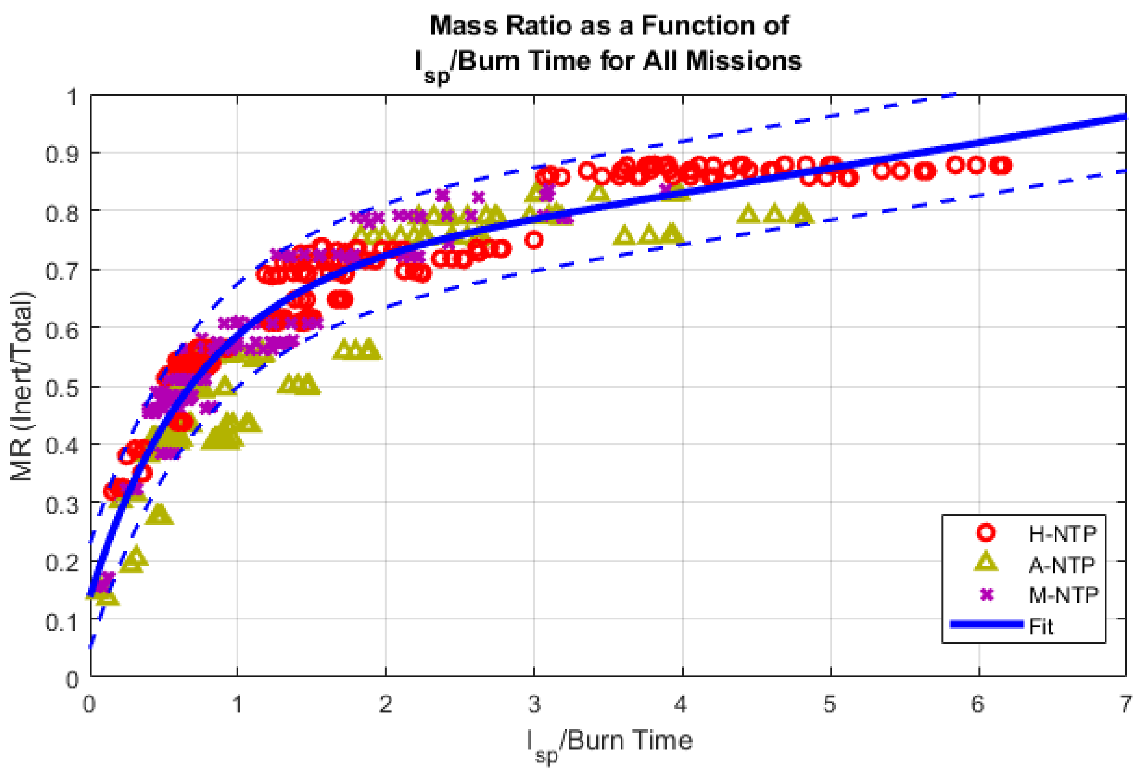

Figure 5: Mass Ratio as a Function of the Specific Impulse to Burn Time Ratio

$$MR = f_1\left(\frac{I_{sp}}{t_{burn}}\right) = 0.6865\exp\left(0.0482\frac{I_{sp}}{t_{burn}}\right) - 0.5482\exp\left(-1.4137\frac{I_{sp}}{t_{burn}}\right) \qquad \text{Eq. 96}$$

Using the Buckingham Π theorem, a dimensionless engine performance parameter was determined that incorporates the engine thrust, engine dry mass, specific impulse, and the ΔV it is to produce via $\frac{F_{Eng}I_{sp}}{m_{Eng}\Delta V}$. This is essentially a ratio between engine impulse to the change in momentum of the engine. Since this is a flight test, the engine can be seen as the payload, therefore, the bottom term could be iterpretted as the change in momentum of the payload. Therefore, lower values of this engine parameter would be preferable as this would mean that lower impulse yields higher payload final momentum.

The engine thrust, engine mass, specific impulse, and ΔV are all parameters that can be specified by the design engineer. Selecting a specific impulse will invariantly select the propellant and engine thermal performance while selecting the ΔV will size the system. The engine thrust and mass are a coupled pair of parameters which also impact the burn time. If the dimensionless engine performance parameter is plotted against ratio of specific impulse to burn time as shown in Figure 6, the result is described by function f_2 shown in Eq. 97 which has ±10% bounds to emncompass all the cases. Similar to the plot in Figure 5, higher $\frac{I_{sp}}{t_{burn}}$ values are preferable in terms of effective propellant usage.

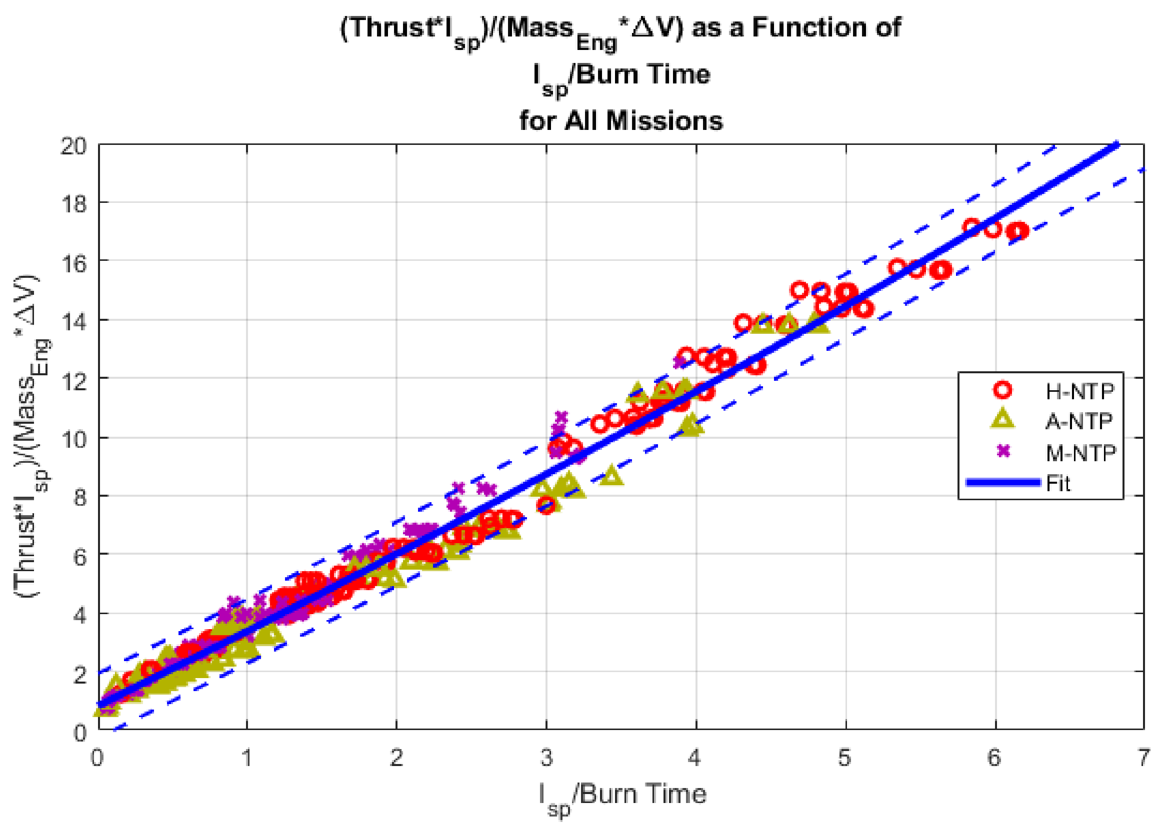

Figure 6: Specific Impulse to Burn Time Ratio as a Function of the Dimensionless Engine Performance Parameter

$$\frac{F_{Eng} I_{sp}}{m_{Eng} \Delta V} = f_2\left(\frac{I_{sp}}{t_{burn}}\right) = -756.6396\exp\left(0.0153\frac{I_{sp}}{t_{burn}}\right) + 757.4747\exp\left(0.0186\frac{I_{sp}}{t_{burn}}\right) \quad \text{Eq. 97}$$

A combination of the relations shown in Figure 5 and Figure 6 could also be made and display the vehicle mass ratio as a function of the dimensionless engine performance parameter as shown in Figure 7. This relationship described by function f_3 shown in Eq. 98 with a ±10% bound also follows a trend with a "knee in the curve" at an engine performance value of 4 which also corresponds to a mass ratio of 0.6 which is similar to that of Figure 5. If cross referenced with Figure 6, this corresponds to a $\frac{I_{sp}}{t_{burn}}$ value of 1 which states that the "knee in the curve" is the same across these three parameters. This area could be a balance between high mission performance and test utility for which both H-NTP and M-NTP fit closer than A-NTP. At this location, both Figure 5 and Figure 7 show that A-NTP has a lower vehicle mass ratio than the trend bounds. This signifies that in the context of a flight test, lower dry mass yields more propellant mass which yields more burn time and therefore testing time. Which, by that logic, shows that A-NTP may have an advantage over the other propellants for the purposes of a flight test, provided that using hydrogen on the flight test is not a requirement.

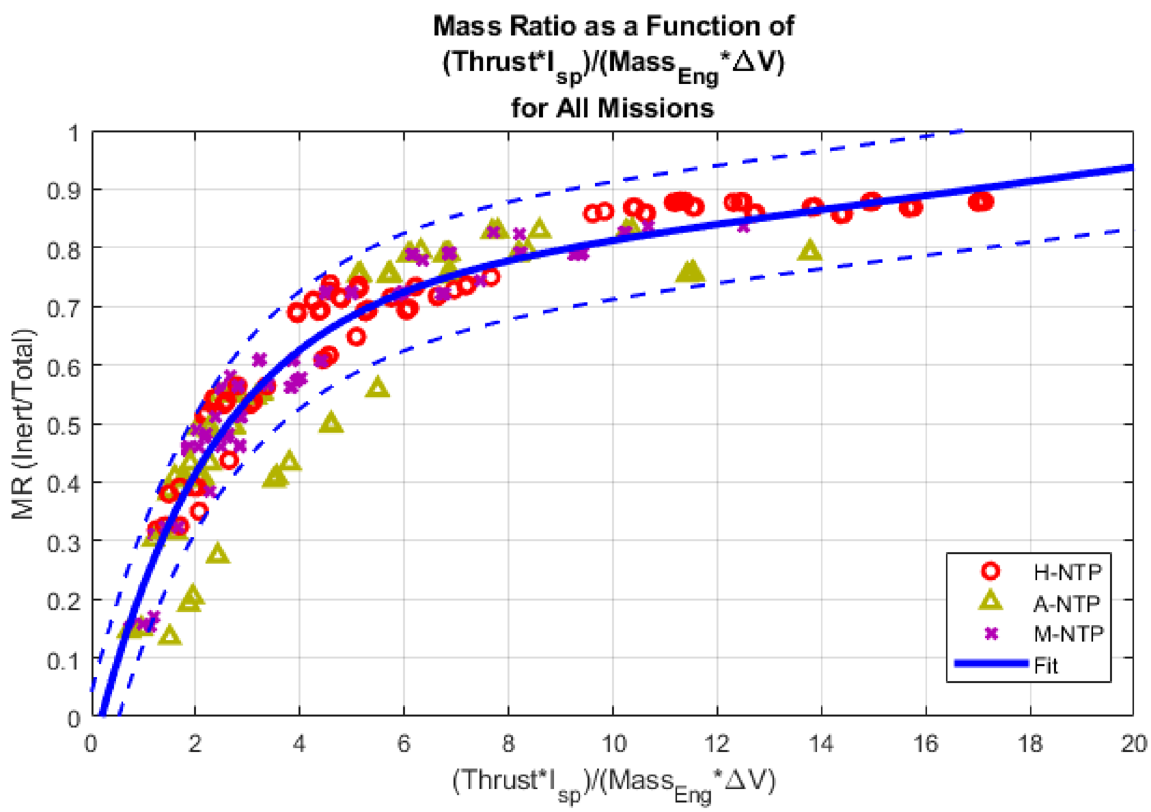

Figure 7: Mass Ratio as a Function of the Dimensionless Engine Performance Parameter

$$MR = f_3\left(\frac{F_{Eng} I_{sp}}{m_{Eng} \Delta V}\right) = 0.7198\exp\left(0.0132\frac{F_{Eng} I_{sp}}{m_{Eng} \Delta V}\right) - 0.7860\exp\left(-0.4438\frac{F_{Eng} I_{sp}}{m_{Eng} \Delta V}\right) \quad \text{Eq. 98}$$

Since dimensionless parameters do not have any dimensions associated with them, they can be lumped together as seen in some convective heat transfer coefficient correlations [12–14]. One such useful combination that was found during this research is the dimensionless engine performance parameter modified by the mass ratio and expressed as a function of specific impulse to burn ratio as shown in Figure 8. This shows a functional relationship among all three dimensionless parameters which is described by Eq. 99. This relationship appears to have a very similar shape to that shown in Figure 6, however, the modification of the dimensionless engine performance parameter by the mass ratio makes the curve take a more concave shape with similar values on the y-axis. This is because the mass ratio increases rapidly at specific impulse to burn time ratios between 0 and 2, and then steadily rises as was shown in Figure 5.

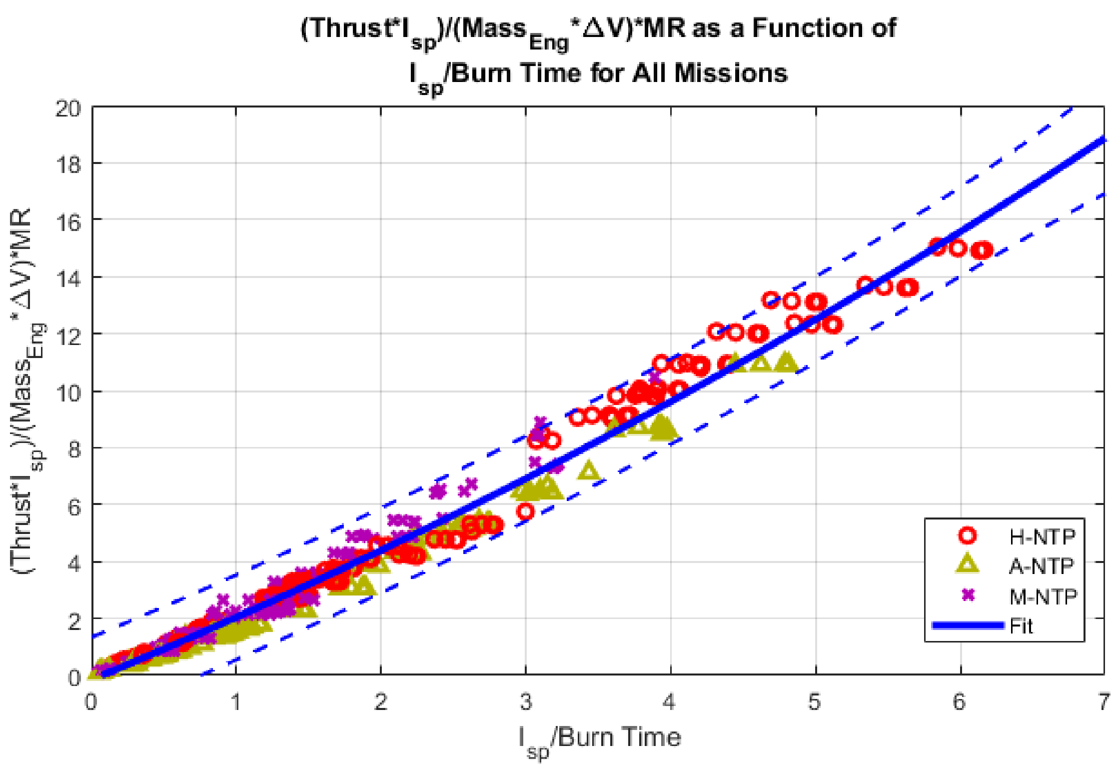

Figure 8: Dimensionless Engine Performance Parameter Modified by the Mass Ratio as a Function of Specific Impulse to Burn Time Ratio

$$\frac{F_{Eng} I_{sp}}{m_{Eng} \Delta V} MR = f_4\left(\frac{I_{sp}}{t_{burn}}\right) = -886.5472\exp\left(0.0346\frac{I_{sp}}{t_{burn}}\right) + 886.3960\exp\left(0.0369\frac{I_{sp}}{t_{burn}}\right) \quad \text{Eq. 99}$$

When the three dimensionless parameters are plotted on separate axes, a 3D curve emerges as shown in Figure 9. This is a parametric curve with the parameter being the specific impulse to burn ratio meaning that both the mass ratio and the dimensionless engine performance parameter are functions of it. These functions were already described by Eq. 96 and Eq. 97, respectively, and when combined, offer a more complete view of the relations which appear to resemble a rising spiral with curvature that increases exponentially.

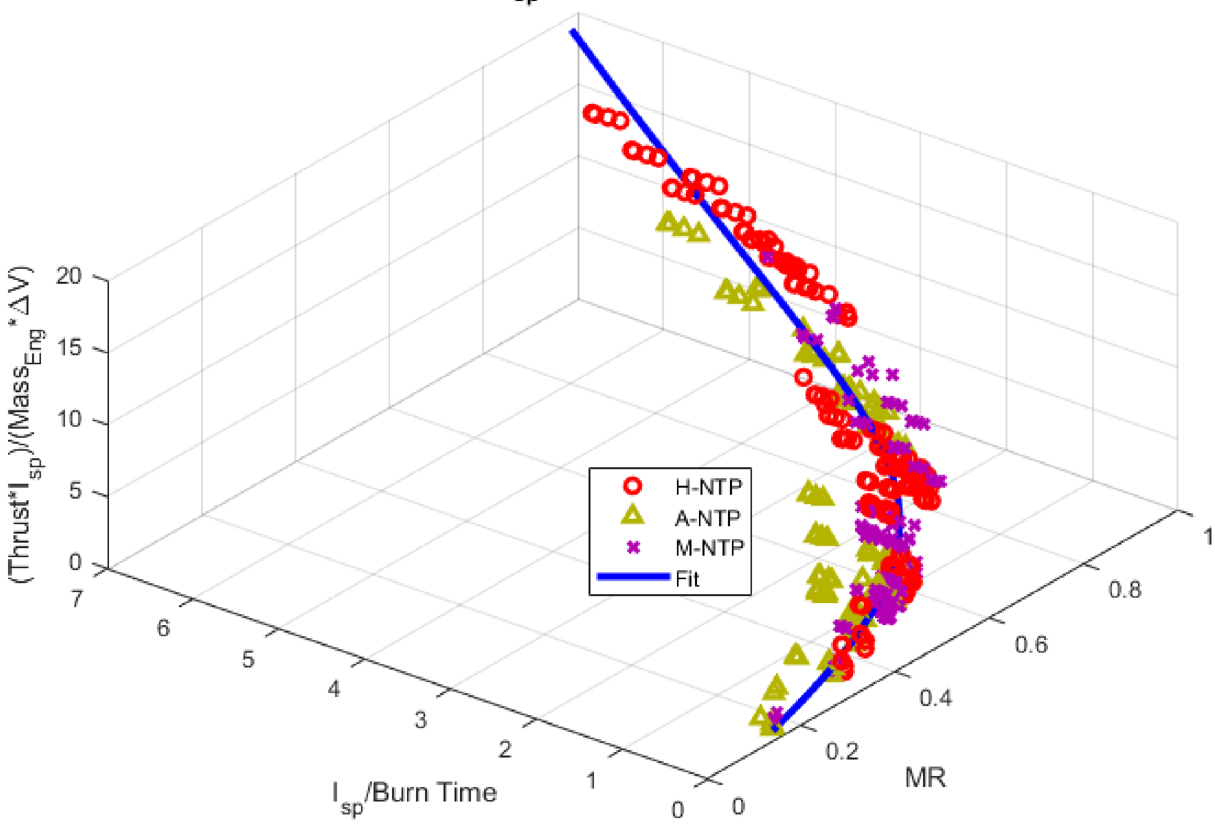

Figure 9: Dimensionless Engine Performance Parameter as a Function of Mass Ratio and Specific Impulse to Burn Time Ratio

IV.B.2 Solutions Based on Dimensionless Parameters

A way to use these equations and relations would be to select the parameters for which requirements are known with three parameters to remain as unknowns. Although for an analytical solution three equations would be necessary to solve for each unknown, in a numerical solution space of transcendental equations, the analytical rules and guidelines tend to breakdown for an ill-conditioned system and a seemingly over-constrained system of four equations is required to *reliably* solve for each of the three unknown variables. By *reliably*, it is meant that the obtained solution can be plugged back into this set of equations and retrieve the exact input parameters regardless if there are small changes in the initial conditions. If only three equations are used, the numerical solution will often yield solutions corresponding to a local minimum depending on the algorithm, solver, and initial guesses used given the ill-conditioned nature of the system. By overconstraining the solution space, a repeatable solution is guaranteed to be found by making the problem essentially well-conditioned. [15,16] The equations used correspond to those found in Eq. 96 through Eq. 99. The parameters which can be chosen are summarized in Table 5.

Table 5: Summary of Parameters

Parameter	Definition	Units
F_{Eng}	Engine thrust class	N
I_{sp}	Specific impulse	s
m_{Eng}	Engine mass	kg
ΔV	Change in velocity	m
t_{burn}	Burn time	s
MR	Inert mass to initial wetted mass ratio	-

IV.B.2.i Determining the Specific Impulse from a Desired Burn Time and Engine Thrust/Mass Class

Example 1 of using these parameters would be to design a mission with a question of "Which propellant should be used?" given an engine with a thrust of 10 klbf (44,482.2 N) and a mass of 3,000 kg capable of providing a total burn time or test time of 1,000 seconds. Here, the unknowns are the propellant and therefore the specific impulse, ΔV, and mass ratio. When Eq. 96 through Eq. 99 are solved for the specific impulse, ΔV, and mass ratio, the solutions yield values of 439 seconds, 3,353 m/s, and 0.4065, respectively. The most important value from this is the specific impulse which will require the use of either a high temperature A-NTP engine that promotes ammonia thermolysis with a nominal specific impulse of at least 450 seconds or an M-NTP engine with a nominal specific impulse of 494 seconds that promotes pyrolysis. In either case, a dissociated alternative propellant would be the preferable option in this case. The corresponding $\frac{I_{sp}}{t_{burn}}$ and dimensionless engine performance parameter are 0.4391 and 1.9420, respectively. When taken with the mass ratio of 0.4065, the solution is on the bottom left of the plots in Figure 5 through Figure 8 and towards the bottom of the curve in Figure 9 to provide perspective to its location in the design space.

When the entire solution space of these values is analyzed as shown in Figure 10, there appears to be a region between a burn time of 200 to 2000 seconds where the dimensionless parameters remain the same and the specific impulse varies linearly. This states that there is no effect from changing the engine thrust and mass class from a mission perspective at low burn times. However, the ΔV will be affected according to both the burn time and engine thrust and mass class. For desired burn times between 2000 and 4000 seconds, H-NTP is the dominant propellant and reduces its breadth of engine thrust and mass class applicability as the burn time increases. As the burn time is increased, lower engine thrust to engine mass ratios optimize to higher specific impulse values, however, they yield a lower ΔV given the required cryocooler and associated tank masses to store the higher performing propellant. Beyond burn times of 4000 seconds, the ΔV is maximized and propellants with lower specific impulse are favored with the lowest specific impulse attributed to engines with the highest thrust to mass ratio. This analysis states that there are three regions according to the desired burn time that will select the best propellant which include: (1) up to 2000 seconds with linearly increasing specific impulse according to burn time, (2) between 2000 and 4000 seconds where H-NTP is mostly preferable, especially at lower engine thrust to mass values, and (3) above 4000 seconds where increasing burn time requires propellants with lower specific impulse with higher engine thrust to mass ratios preferring the lowest specific impulse propellants.

There are regions where the required propellant specific impulse is in between H-NTP and A/M-NTP engines suggesting that a fourth propellant option would be required that has not been evaluated in this study. In such cases, there are three options: (1) the reader should select a propellant that would have an expected performance between H-NTP and A/M-NTP engines, (2) the thrust and mass class of the engine would need to be changed to yield either H-NTP or A/M-NTP equivalent specific impulse values, or (3) the desired burn time would need to be changed. Other options could be to operate the A/M-NTP engines at higher chamber temperatures to reach the required specific impulse values. Decreasing the operating temperature of H-NTP engines will not yield the desired burn time and result in a solution space where the engine parameters including the specific impulse are known. This solution space is the subject of the next section.

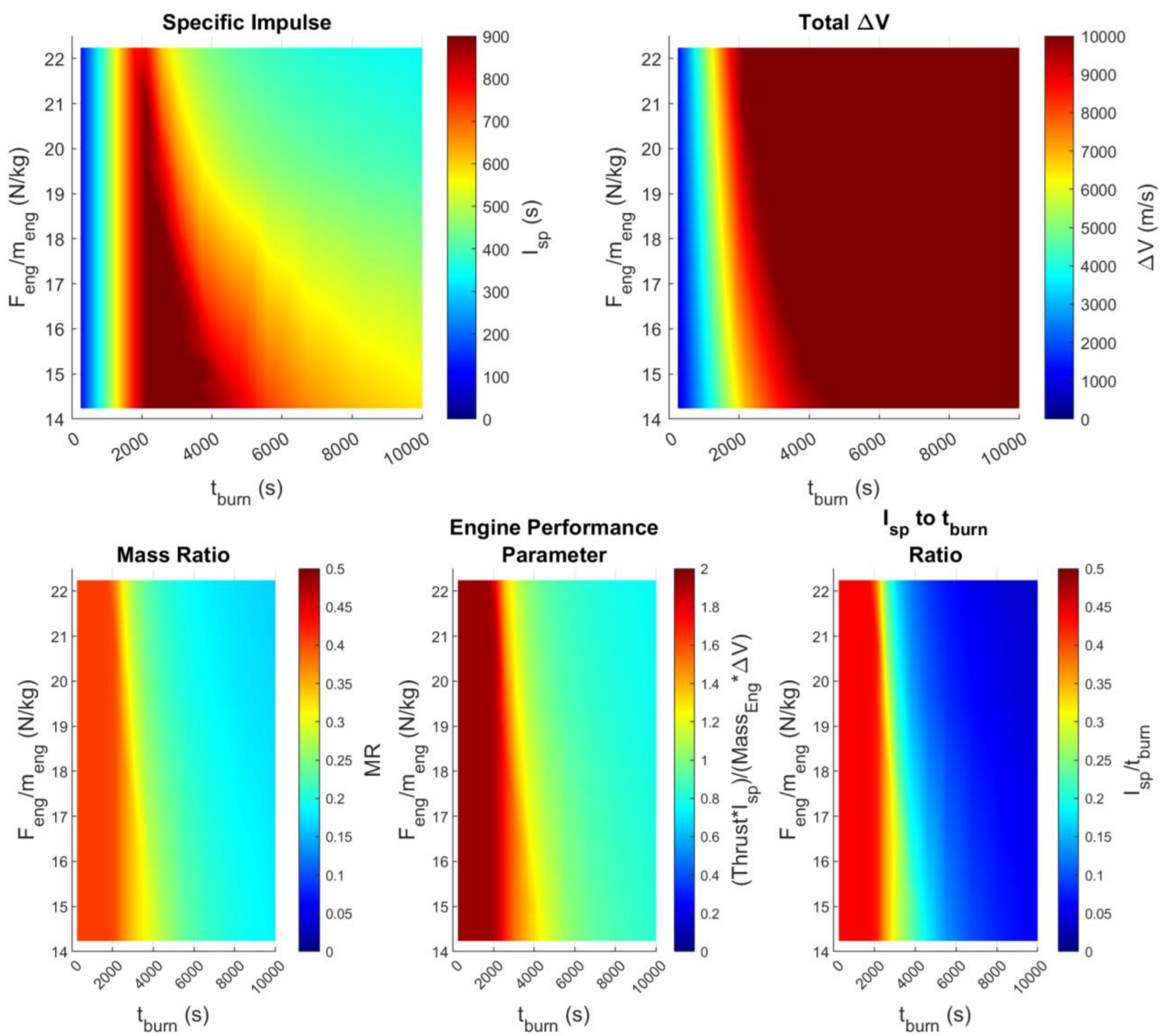

Figure 10: Performance Parameters Given Burn Time and an Engine Thrust/Mass Pair

IV.B.2.ii Determining the Minimum Burn Time from a Known Engine Design

Example 2 of using these parameters would be to ask, “How much test time is possible to obtain from a H-NTP 15 klbf engine that has an effective specific impulse of 775 seconds?” This involves selecting a system with a known propellant and engine definition. The engine definition in this case is known and defined by an effective mission specific impulse of 775 seconds produced by an engine with a thrust of 15 klbf (66,723.3 N) and a mass of 3,400 kg. The unknowns are the burn time, ΔV, and mass ratio which can be determined by solving equations Eq. 96 through Eq. 99 simultaneously and numerically thus yielding values of 1765 seconds or 29.42 minutes, 7,865 m/s, and 0.4065, respectively. The corresponding $\frac{I_{sp}}{t_{burn}}$ and dimensionless engine performance parameter are 0.4391 and 1.9420, respectively, which are the same as those in the previous point example.

Unlike the previous example, when the entire design space for the specific impulse and engine thrust and mass class is evaluated as shown in Figure 11, the trends are seemingly radically different. However, when compared against Figure 10, this is a subset of the entire solution space which is the zoomed in view of the region where the burn time is up to 2000 seconds. Therefore, when this system of equations is asked to evaluate a particular engine design, they will return the MINIMUM burn time that can be produced yielding a conservative result. Here, the dimensionless parameters are constant and the produced ΔV results in higher values with engine thrust to mass ratio values. Furthermore, it is possible to get burn times larger than 2000 seconds when the system is optimized toward the specific desired burn time value. However, this optimization criterion is the same as that of Example 1.

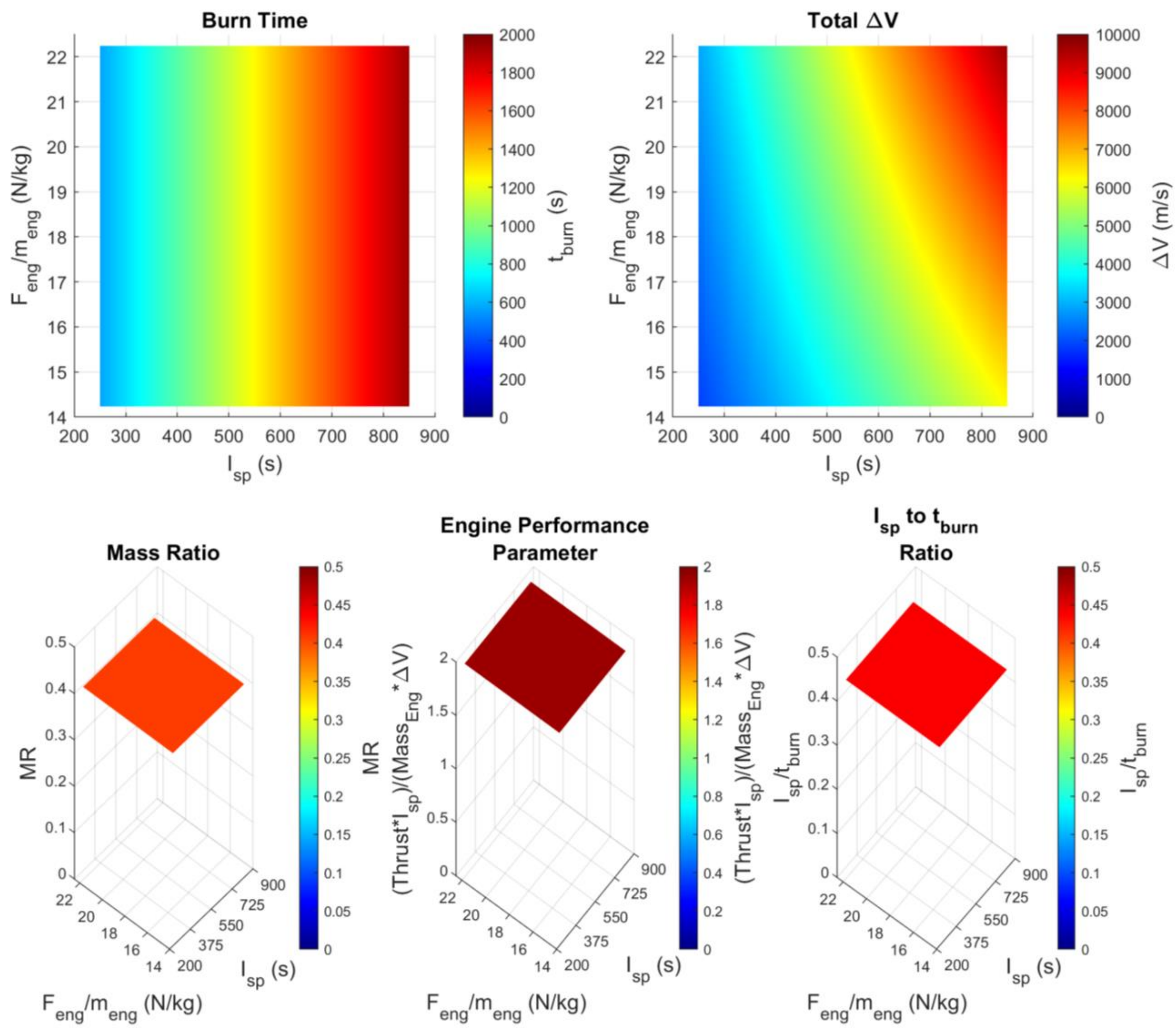

Figure 11: Performance Parameters Given Average Specific Impulse and an Engine Thrust/Mass Pair

V. CONCLUSION

Following the first Nuclear Thermal Propulsion (NTP) system test, also known as DRACO, the next NTP system to be developed would be the 1st Generation NTP system. Given the inherent propellant flexibility of the monopropellant NTP system, analysis was conducted to determine the performance of different vehicle configurations utilizing hydrogen (H-NTP), ammonia (A-NTP), and methane (M-NTP) as propellants launched onboard commercial launch vehicles. Transient engine performance was considered for all three propellants that was informed by the X-NTP model. Physics models were developed that sized the vehicle system using Master Equipment List (MEL) parameters that allow complete flexibility in choosing the mission architecture, engine, propellant, and essential spacecraft systems. A matrix of different mission classes and vehicle configurations was outlined that attempted to cover the design space of a 1st Generation NTP system that would be launched as a single stage vehicle. Each combination of the matrix elements was run and provided insight into different trends and showed that three equations could be used to provide a high-level mission design capability to determine different vehicle and mission configuration parameters based on the designer's preferences on what should be tested. This study does not attempt to make a recommendation rather provide the tools for the reader to select their own configuration based on their needs.

The matrix did not consider payload mass for any of the mission classes given that this is fundamentally a flight test. Therefore, the engine itself could be viewed as the payload. This matrix aimed to explore various propellant options, engine architectures, and mission scopes. The goal of each combination of matrix parameters was to fit everything on a single commercial launch vehicle, which is why the SLS launch vehicle variants were not included. The results of the matrix showed that beyond the propellant selection type, the launch vehicle selection, which included Starship, New Glenn, Vulcan, Falcon 9 (recoverable), and Falcon Heavy (recoverable), was a primary driving factor in the test vehicle's capabilities.

Four mission classes were evaluated which included single burn missions performing maneuvers having a ΔV of 1 km/s and 2.5 km/s followed by 2-burn and 4-burn missions that aimed to exhaust the launch vehicles volume or mass limitations, which ever was encountered first. Both single burn missions showed that A-NTP configurations provided the lowest dry mass given that ammonia had the highest density with comparable performance to M-NTP systems and no requirement for cryocoolers. Configurations that used the Starship and New Glenn launch vehicles required the highest overall dry mass across all missions given their large payload bay diameters. The multi-burn missions did not significantly differ from each other except that the 4-burn had a marginally lower total ΔV capability given that the engine spent more propellant during engine transients and cooldown than the 2-burn mission. In all cases, the NTP systems with the lowest thrust class and corresponding lowest engine mass had the longest burn time which could be very useful as a testing platform to increase the time for data accumulation. Both A-NTP and M-NTP systems can provide the longest and shortest burn times depending on the launch vehicle used while H-NTP systems tended to cluster together in the middle. Across the multi-burn cases, H-NTP systems were found to be largely volume limited while A-NTP and M-NTP systems were largely found to be mass limited.

An analysis was performed based on all the data points obtained from running the cases of the matrix that developed relations among dimensionless parameters. These parameters included the mass ratio of inert mass to initial wetted mass, ratio of specific impulse to burn time, and a dimensionless engine parameter which effectively was the ratio of impulse to engine momentum. These relationships found the "knees-in-the-curves" that could be a significant point of reference for the designer as they indicate a change in the trend which is located at a specific impulse to burn time ratio of 1, a mass ratio of 0.6, and an engine performance parameter of 4.

ACKNOWLEDGMENTS

This work was supported by NASA's Space Technology Mission Directorate (STMD) through the Space Nuclear Propulsion (SNP) project. This work was funded under Contract No. 80LARC23DA003.

REFERENCES

[1] Robbins, W. H., and Finger, H. B., “An Historical Perspective of the NERVA Nuclear Rocket Engine Technology Program,” NASA Contractor Report NASA-CR-187154, Analytical Engineering Corporation, July 1991.

[2] Nikitaeva, D., and Thomas, D. L., “Alternative Propellant Nuclear Thermal Propulsion Engine Architectures,” *Journal of Spacecraft and Rockets*, 2022, pp. 1–11. https://doi.org/10.2514/1.A35289

[3] Nikitaeva, D., Smith, C., D., and Duchek, M., “Methane-Based Nuclear Thermal Propulsion Engine Considerations,” presented at the Nuclear Emerging Technologies for Space 2025, Huntsville, AL, 2025.

[4] Nikitaeva, D., Smith, C. D., and Duchek, M., “Engine Cycle Comparison for Alternative Propellant Nuclear Thermal Propulsion Engines,” presented at the ASCEND 2023, Las Vegas, Nevada, 2023. https://doi.org/10.2514/6.2023-4715

[5] Duchek, M. E., Nikitaeva, D., Harnack, C., Grella, E., and Greenhalge, S., “Parametric Modeling of NTP Engine Performance for a Crewed Mars Mission,” presented at the ASCEND 2023, Las Vegas, Nevada, 2023. https://doi.org/10.2514/6.2023-4717

[6] Williams, J., Senent, J. S., Ocampo, C., and Davis, E. C., “Overview and Software Architecture of the Copernicus Trajectory Design and Optimization System,” presented at the 4th International Conference on Astrodynamics Tools and Techniques, Madrid, Spain, 2010.

[7] Greenhalge, S., and Duchek, M., “Concept of Operations of Cryogenic Fluid Management for Nuclear Thermal Propulsion,” presented at the AIAA SciTech 2025, Orlando, FL, 2025.

[8] Gustafson, J., Kreicicki, M., Swanson, R., Zilka, B., and Witter, J. K., “Space Nuclear Propulsion Fuel and Moderator Development Plan Conceptual Testing Reference Design,” presented at the Nuclear Emerging Techologies for Space, Virtual Event, 2021.

[9] Nikitaev, D., “Implications of Alternative In-Situ Propellants Used in Nuclear Thermal Propulsion Engines,” Dissertation. University of Alabama in Huntsville, Huntsville, AL, 2021.

[10] Duchek, M., Harnack, C., Nikitaeva, D., and Greenhalge, S., “KEY PERFORMANCE PARAMETERS FOR AN OPERATIONAL CIS-LUNAR NTP VEHICLE,” presented at the JANNAF 2024, Oklahoma City, OK, 2024.

[11] Stone, C., “Opinion & Analysis Global, Space To Give US Satellites a Chance against Rivals, Pursue Safe Nuclear Propulsion,” *Breaking Defense*, Feb 22 2022.

[12] Mills, A. F., and Coimbra, C. F. M., “Heat Transfer,” 2016.

[13] Incropera, F. P., and DeWitt, D. P., “Fundamentals of Heat and Mass Transfer,” J. Wiley, New York, 2002.

[14] Çengel, Y. A., and Ghajar, A. J., “Heat and Mass Transfer: Fundamentals & Applications,” McGraw-Hill, New York, 2011.

[15] Hass, J., Heil, C., Bogacki, P., Weir, M. D., and Thomas, G. B., “University Calculus: Early Transcendentals,” Pearson Education, Inc, Hoboken, NJ, 2020.

[16] Kreyszig, E., Kreyszig, H., and Norminton, E. J., “Advanced Engineering Mathematics,” John Wiley, Hoboken, NJ, 2011.